# Technical Report
# ONR Grant Number N000140810531
# Estimating the Effects of Damping Treatments on the Vibration of Complex Structures

J. Gregory McDaniel, Associate Professor
Kyle Bridgeo, Research Assistant
Hande Öztürk, Research Assistant
Department of Mechanical Engineering
Boston University
110 Cummington Mall
Boston, Massachusetts 02215
jgm@bu.edu

September 26, 2012

# REPORT DOCUMENTATION PAGE

*Form Approved*
*OMB No. 0704-0188*



| 1. REPORT DATE *(DD-MM-YYYY)* | 2. REPORT TYPE | 3. DATES COVERED *(From - To)* |
|---|---|---|
| 08-15-2012 | Final | 02/07/2008-04/30/2012 |

**4. TITLE AND SUBTITLE**

Estimating the Effects of Damping Treatments on the Vibration of Complex Structures

**5a. CONTRACT NUMBER**
N000140810531

**5b. GRANT NUMBER**
N000140810531

**5c. PROGRAM ELEMENT NUMBER**

**6. AUTHOR(S)**

J. Gregory McDaniel

**5d. PROJECT NUMBER**

**5e. TASK NUMBER**

**5f. WORK UNIT NUMBER**

**7. PERFORMING ORGANIZATION NAME(S) AND ADDRESS(ES)**

Trustees of Boston University
881 Commonwealth Avenue
Boston Ma, 02215

**8. PERFORMING ORGANIZATION REPORT NUMBER**

**9. SPONSORING / MONITORING AGENCY NAME(S) AND ADDRESS(ES)**

Office of Naval Research
875 North Randolph Street
Arlington, VA 22203-1995

**10. SPONSOR/MONITOR'S ACRONYM(S)**
ONR

**11. SPONSOR/MONITOR'S REPORT NUMBER(S)**

**12. DISTRIBUTION / AVAILABILITY STATEMENT**

Approved for public release.

**13. SUPPLEMENTARY NOTES**

**14. ABSTRACT**

Damping treatments are used in most Naval platforms to reduce noise and vibration, and are therefore critical to structural acoustic performance. However, the complexity of naval structures often limits one's ability to accurately estimate the structural acoustic performance of a given damping treatment. As a result, some damping treatments represent a significant cost without a significant benefit. Costs include initial material and labor as well as routine maintenance that involves the replacement of treatments due to inspection of the underlying structure (see MIL-STD-2148). The importance of this research lies in the possibility of identifying which damping treatments may be permanently removed or never installed without sacrificing substantial performance, thus significantly reducing the cost of naval platforms. The research has achieved this by developing a set of processing techniques for experimental data and structural acoustic models.

**15. SUBJECT TERMS**

damping, vibration, dynamics, thermal imaging

| 16. SECURITY CLASSIFICATION OF: | | | 17. LIMITATION OF ABSTRACT | 18. NUMBER OF PAGES | 19a. NAME OF RESPONSIBLE PERSON |
|---|---|---|---|---|---|
| a. REPORT | b. ABSTRACT | c. THIS PAGE | Unclassified Unlimited | 61 | ONR |
| Unclassified (U) | Unclassified (U) | Unclassified (U) | | | 19b. TELEPHONE NUMBER *(include area code)* 703-696-2607 |

## Abstract

Damping treatments are used in most Naval platforms to reduce noise and vibration, and are therefore critical to structural acoustic performance. However, the complexity of naval structures often limits one's ability to accurately estimate the structural acoustic performance of a given damping treatment. As a result, some damping treatments represent a significant cost without a significant benefit. Costs include initial material and labor as well as routine maintenance that involves the replacement of treatments due to inspection of the underlying structure (see MIL-STD-2148). The importance of this research lies in the possibility of identifying which damping treatments may be permanently removed or never installed without sacrificing substantial performance, thus significantly reducing the cost of naval platforms. The research has achieved this by developing a set of processing techniques for experimental data and structural acoustic models.

# Contents

# List of Figures

# Chapter 1

# Project Overview

The goal of this project has been to investigate the effects of damping treatment on complex structures. This work resulted in the following accmplishments, which are detailed in the following chapters:

**Application of the Ritz Method to optimization of vibrating structures** This work showed how damping may be optimally placed to reduce vibration levels. The key contribution here was the discovery of efficient numerical models for evaluating cost functions, which enabled exhaustive searches over design combinations.

**Optimizing the spatial distribution of damping in structures with boundary damping** This work investigated the effect of boundary damping on the optimization of damping placement. It produced analytical and numerical results that illustrated the importance of incorporating boundary damping in models used for optimization.

**Thermal imaging techniques for evaluation of vibrational damping** The recent availability of thermal video cameras with resolutions of approximately 0.025°C prompted an investigation to see if this technology could be used to detect damping *in situ* by measuring temperature increases caused by heating of the damping material. This work defined parameter ranges over which the approach would be accurate.

## 1.1 Technology transfer

The principal investigator met frequently with engineers at Carderock, Electric Boat and Newport News to share results of the research. I August of 2011, he was invited by Admiral Kirkland Donald to participate in a trip aboard the USS Toledoa (See Figure 1.2), which provided a unique opportunity to discuss the research with the Navy, but more importantly to better understand the technology needs of the fleet.

## 1.2 Project participants

The project included contributions from the following participants

- Professor J. Gregory McDaniel

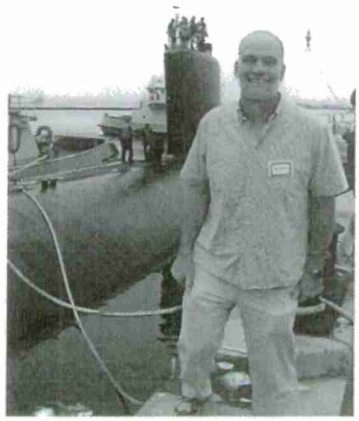

Figure 1.1: Principal Investigator, Professor J. Gregory McDaniel, preparing to board the USS Toledo in August of 2011.

- Kyle Bridgeo, MS student currently with structural dynamics group at Boeing
- Hande Özturk, MS student currently in PhD program at Columbia University
- Thom Howe, undergraduate student currently at Boston University
- Sarah Provencher, undergraduate student currently at Boston University

## 1.3 Summary of publications and presentations

The following are conference presentations with refereed abstracts:

- "Application of time windowing to spatial maps of damping," Hande Öztürk and J. Gregory McDaniel. Abstract published in the Journal of the Acoustical Society of America, Vol. 27, No. 3, pp. 1888-1889, March 2010. Presented at the 159th ASA Meeting/NOISE-CON 2010, Baltimore, Maryland, April 21, 2010.
- "Spatial mapping of modal damping in vibrating plates," Hande Öztürk and J. Gregory McDaniel, presented at the 158th Meeting of the Acoustical Society of America, San Antonio, Texas October 28, 2009.
- "Spatial maps of modal damping from frequency response measurements. J. Gregory McDaniel, Craig Boucher, and Hande Öztürk, presented at the 157th Meeting of the Acoustical Society of America, Portland, Oregon, May 19, 2009.

The following are invited lectures with refereed papers:

1. "Application of the Ritz Method to the Optimization of vibrating structures," J. Gregory McDaniel and Andrew S. Wixom, Proceedings of Internoise 2012/ASME NCAD meeting August 19-22, 2012, New York City, NY, USA, Paper IN12-1211.

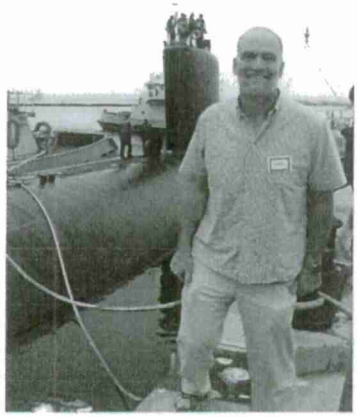

Figure 1.2: Principal Investigator, Professor J. Gregory McDaniel, preparing to board the USS Toledo in August of 2011.

2. "Optimizing the spatial distribution of damping in structures with boundary damping," J. Gregory McDaniel and Andrew S. Wixom, Proceedings of Internoise 2012/ASME NCAD meeting August 19-22, 2012, New York City, NY, USA, Paper IN12-1206.

The following is an MS Thesis: *The Use of Thermal Imaging Techniques for Evaluation of Constrained Layer Treatments for Vibrational Damping*, Kyle Robert Bridgeo, Department of Mechanical Engineering, Boston University, 2009.

# Chapter 2

# Application of the Ritz Method to the optimization of vibrating structures

## 2.1 Introduction

This work presents an application of the Ritz Method to the optimization of vibrating structures. The optimization problems considered here involve local design choices made in various regions of the structure in hopes of improving the vibration characteristics of the structure. In order to find the global optimum, one must perform an exhaustive search over all combinations of such choices. Even a modest number of design choices may give rise to a large number of combinations, so that an exhaustive search becomes computationally intensive. In the present work , the Ritz Method is employed to efficiently compute cost functions related to the vibration characteristics of the structure. Since the Ritz Method is based on integral expressions of the potential and kinetic energies of the structure, one may naturally divide these integrals over regions of the structure. In doing so, the concept of substructuring appears naturally in the formulation without explicitly considering boundary conditions between regions. This advantage, combined with the well-known convergence properties of the Ritz Method, provide for a computationally efficient approach for optimization problems. Numerical examples related to the optimization of a vibrating plate illustrate the approach.

In many applications, one wishes to design a vibrating structure in order to produce desired vibrational characteristics. For example, one may wish to design a vibrating plate to either minimize or maximize the amount of sound radiated by the plate. The present work addresses situations where the designer has the opportunity to introduce a number of design modifications that involve local modifications to the structure and, due to cost and complexity, may only choose a subset of these modifications. Therefore, one is faced with the question of which combination of modifications should be chosen to minimize a cost function related to vibration, acoustic radiation, or both. The present work proposes a method to find the optimal set of design modifications that minimize a cost function. The method involves an exhaustive search of all combinations and uses the Ritz Method as a computationally efficient means of computing the cost function for each combination. A significant advantage of this approach over others is the guarantee that a global minimum in the cost function has been found. For clarity, the present work focuses on the optimization of a vibrating plate, however the approach is by no means limited to this case.

Much work has been done on the optimization of vibrating structures by varying their topology

and material properties. For example, Maeda *et al* [2] employed a topology optimization approach in concert with a finite element representation of the structure. This approach found the distribution of material properties that minimized a cost function involving the eigenvalues of the structure. Recently, Shu *et al* [3] presented an approach for structural topology optimization using level set method to minimize the frequency response of the structure. Heidari *et al* [4] presented a method to minimize the peak power input to a truss by varying the cross-sectional areas of the truss elements while keeping the total mass of the truss constant. The optimization was formulated as a semidefinite programming problem.

Others have investigated the optimization of vibrating structures by applying patches of damping treatment. Alvelid [5] presented an approach for finding optimal locations and shapes of constrained layer damping treatments in order to minimize the frequency-averaged response of a vibrating plate. This work used the modified gradient method and successively added patches of treatment. Zheng *et al* [6] compared several optimization algorithms for positioning constrained layer damping treatments in order to reduce the response of the odd-numbered vibrational modes that contribute most to the acoustic radiation of the plate. The present work is most similar to the works of Alvelid and Zheng in that it is concerned with partially treated plates, but differs in one important aspect. The present work performs an exhaustive search on all combinations of damping placement and therefore finds the global minimum in the associated cost function.

## 2.2 Ritz Method

The Ritz Method was first published in 1909 [7] and is based on Hamilton's Principle [8, 9]. Applications of the method to the vibrations of beams and bars are given by Ginsberg [10] and Rao [11]. Since the present work involves a vibrating plate in flexure, the Ritz Method is presented here for that case. The kinetic and potential energies of the plate having lateral dimensions $(a, b)$ are

$$T = \frac{1}{2}\int_0^b \int_0^a \rho(x,y)h(x,y)\left(\frac{\partial w}{\partial t}\right)^2 dxdy, \tag{2.1}$$

$$U = \frac{1}{2}\int_0^b \int_0^a D(x,y)\left\{\left(\frac{\partial^2 w}{\partial x^2}+\frac{\partial^2 w}{\partial y^2}\right)^2 \right. \tag{2.2}$$

$$\left. - \; 2(1-\nu)\left[\frac{\partial^2 w}{\partial x^2}\frac{\partial^2 w}{\partial y^2} - \left(\frac{\partial^2 w}{\partial x \partial y}\right)^2\right]\right\} dxdy, \tag{2.3}$$

where $h(x,y)$ is the thickness and $\rho(x,y)$ is the mass density. The bending ridigity is $D(x,y) = E(x,y)h^3(x,y)/[12(1-\nu(x,y)^2)]$ where $E$ is the Young's modulus and $\nu$ is the Poisson's ratio. The Ritz Method approximates the displacement as

$$w(x,y,t) \approx \sum_{n=1}^{N} q_n(t)\phi_n(x,y,), \tag{2.4}$$

where the $q_n(t)$ are generalized coordinates and the $\phi_n(x,y)$ are admissible functions that satisfy the geometric boundary conditions. Substitution of this expression into the kinetic and potential

energy expressions yields the quadratic sums

$$T = \frac{1}{2}\sum_{m=1}^{N}\sum_{n=1}^{N} M_{mn}\dot{q}_m(t)\dot{q}_n(t), \tag{2.5}$$

$$V = \frac{1}{2}\sum_{m=1}^{N}\sum_{n=1}^{N} K_{mn}q_m(t)q_n(t). \tag{2.6}$$

where the elements of the mass and stiffness matrices are

$$M_{mn} = \int_0^b\int_0^a \rho(x,y)h(x,y)\phi_m(x,y)\phi_n(x,y)\,dxdy, \tag{2.7}$$

$$K_{mn} = \int_0^b\int_0^a D(x,y)k_{mn}(x,y)\,dxdy, \tag{2.8}$$

and where

$$k_{mn} = \left(\frac{\partial^2\phi_m}{\partial x^2}+\frac{\partial^2\phi_m}{\partial y^2}\right)\left(\frac{\partial^2\phi_n}{\partial x^2}+\frac{\partial^2\phi_n}{\partial y^2}\right) \tag{2.9}$$

$$- \; 2(1-\nu)\left(\frac{\partial^2\phi_m}{\partial x^2}\frac{\partial^2\phi_n}{\partial y^2}-\frac{\partial^2\phi_m}{\partial x\partial y}\frac{\partial^2\phi_n}{\partial x\partial y}\right) \tag{2.10}$$

The Lagrangian is

$$\mathcal{L} = T - V \tag{2.11}$$

and obeys the Euler-Lagrange equation,

$$\frac{d}{dt}\left(\frac{\partial\mathcal{L}}{\partial\dot{q}_n}\right)-\frac{\partial\mathcal{L}}{\partial q_n} = Q_n(t) \tag{2.12}$$

where $Q_n(t)$ is the generalized force found by writing the work due to nonconservative forces,

$$\delta W^{nc}(t) = \sum_{n=1}^{N} Q_n(t)\delta q_n(t) \tag{2.13}$$

The matrix equation of motion is therefore

$$\mathbf{M}\ddot{\mathbf{q}} + \mathbf{K}\mathbf{q} = \mathbf{Q}. \tag{2.14}$$

## 2.3 Formulation for Optimization

Consider that the plate is divided into regions that are assumed to be homogeneous. The properties may, however, change from region to region so that the entire plate is considered to be nonhomogeneous. The mass and stiffness matrices may then be expressed as sums over regions,

$$\mathbf{M} = \sum_{p=1}^{P}\mathbf{M}_p \tag{2.15}$$

$$\mathbf{K} = \sum_{p=1}^{P}\mathbf{K}_p \tag{2.16}$$

where the mass and stiffness matrix for each region is

$$(M_p)_{mn} = \rho_p h_p \iint_{R_p} \phi_m(x,y)\phi_n(x,y)\,dA \tag{2.17}$$

$$(K_p)_{mn} = D_p \iint_{R_p} k_{mn}(x,y)\,dA, \tag{2.18}$$

and where $R_p$ is the area occupied by region $p$. Note that the integrals in the above expressions are independent of the region properties. These means that the integrals may be computed and stored, so that the regional mass and stiffness matrices may be rapidly computed for a given choice of $\rho_p h_p$ and $D_p$. Also note that the dimensions of $\mathbf{M}_p$ and $\mathbf{K}_p$ are $N \times N$ regardless of the size of the region. Therefore, the regional mass and stiffness matrices may simply be added together once choices for $\rho_p h_p$ and $D_p$ have been made for all regions. This observation is the heart of the method. The parameters $\rho_p h_p$ and $D_p$ for the regions are regarded as optimization parameters and the global mass and stiffness matrices are rapidly once these parameters are chosen.

The optimization of the plate proceeds by defining a suitable cost function related to the plate vibration. First consider free vibration characteristics in which $\mathbf{Q} = \mathbf{0}$ in Eqn. 2.14. Seeking solutions of the form $\mathbf{q} = \mathrm{Re}\{\tilde{\mathbf{q}}\exp(i\omega t)\}$ gives the eigenvalue problem

$$\left(-\omega^2\mathbf{M} + \mathbf{K}\right)\tilde{\mathbf{q}} = \mathbf{0}. \tag{2.19}$$

Material damping is included by allowing the Young's modulus to become complex-valued, so that $E_p \to E_p(1+i\eta_p)$ where $\eta_p$ is the material loss factor of the $p$th region. Then the $n$th complex-valued eigenvalue is satisfying Eqn. 2.19 is written as

$$\omega_n^2 = \Omega_n^2\left(1 + i\eta_n\right), \tag{2.20}$$

where $\eta_n$ is the modal loss factor. One cost function is to identify all of the modes in a particular frequency band and attempt to maximize the average modal loss factor, so that the cost function would be

$$f_c = \left(\frac{1}{J}\sum_{j=1}^{J}\eta_j\right)^{-1} \tag{2.21}$$

where $\omega_{min} < \Omega_j < \omega_{max}$.

If the forcing is a known time-harmonic force given by

$$\mathbf{Q}(t) = \mathrm{Re}\left\{\tilde{\mathbf{Q}}\exp(i\omega t)\right\}, \tag{2.22}$$

then the steady-state solution is written as

$$\mathbf{q}(t) = \mathrm{Re}\left\{\tilde{\mathbf{q}}\exp(i\omega t)\right\}, \tag{2.23}$$

where the response amplitude is found from Eqn. 2.14,

$$\tilde{\mathbf{q}} = \left(-\omega^2\mathbf{M} + \mathbf{K}\right)^{-1}\tilde{\mathbf{Q}}. \tag{2.24}$$

The displacement is written as $w(x,y,t) = \mathrm{Re}\left\{\tilde{w}(x,y)\exp(i\omega t)\right\}$, where

$$\tilde{w}(x,y) = \sum_{n=1}^{N}\tilde{q}_n\phi_n(x,y). \tag{2.25}$$

One may wish to minimize the root mean square of response over several locations, in which case a suitable cost function would be

$$f_c = \sqrt{\frac{1}{J}\sum_{j=1}^{J} |\tilde{w}(x_j, y_j)|^2} \tag{2.26}$$

The cost function above can also be extended to include an average over a specified frequency band.

## 2.4 Numerical Examples

In this section, the approach described above is applied to a rectangular plate with free boundaries. These boundary conditions are natural, not geometric, so that the basis functions need not satisfy any particular boundary condition. The work by Oosterhout *et al* [12] has demonstrated that Legendre polynomials have desirable numerical properties when used as basis functions in the Ritz Method. Therefore, the examples will use the basis functions

$$\phi_n(x, y) = P_j(\bar{x})P_k(\bar{y}), \tag{2.27}$$

where

$$\bar{x} = \frac{2x - a}{a} \tag{2.28}$$

$$\bar{y} = \frac{2y - b}{b} \tag{2.29}$$

and $P_n(x)$ is the $n$th degree Legendre polynomial. The orthogonality property

$$\int_{-1}^{1} P_j(x)P_k(x)\,dx = \frac{2}{2n+1}\delta_{jk} \tag{2.30}$$

is responsible for the desirable numerical properties.

The aluminum plate considered, which is shown in Figure 2.1 here has lateral dimensions $a = 1$ m and $b = 0.5$ m, thickness $h = 1$ cm, Young's modulus $E = 70$ GPa, Poisson's ratio $\nu = 0.3$, and mass density $\rho = 2700$ kg/m$^3$.Natural frequencies of the first four non-rigid-body modes are shown in Figure 2.2 and the four modes with the highest natural frequencies below 1000 Hz are shown in Figure 2.3, for the case of an undamped plate.

The plate is divided into 16 regions of equal area having dimensions $a_p = 0.25$ m and $b_p = 0.125$ m. The optimization problem consists of applying a damping treatment to 25% of the plate, such that the material loss factor in that region is assumed to be $\eta_p = 0.1$ and the material damping in other regions is assumed to be $\eta_p = 0.005$.

$$\binom{n}{k} = \frac{n!}{k!(n-k)!}, \tag{2.31}$$

where $n$ is the number of total number of possibilities and $k$ is the number chosen. For the present example, $n = 16$ and $k = 4$, so the total number of combinations is 1,820. As a cost function, we choose to average the modal loss factors according to (2.21) for modes in the frequency range 0-1000 Hz (not including rigid-body modes). This average is shown plotted in Figure 2.4. where


Figure 2.1: Drawing of elastic plate used in numerical simulations.

the configurations have been sorted according to average modal loss factor and labelled with integer combination numbers. Note that the best design has an average modal loss factor of about 0.35 and the worst is about 0.25, which is quite a difference considering that both plates have the same amounts of damping. Figures 2.5 and 2.6 show the configurations for the highest and lowest modal loss factors, which are geometrically very dissimilar. A similar study was performed for 75% coverage and those results are shown in Figure 2.7–2.9.

## 2.5 Conclusions

The present work has presented an approach for optimizing vibrating plates by formulating discrete design decisions and then exhaustively searching all combinations of those decisions. For a vibrating plate, the approach yielded considerably higher performance when the placement of the damping was optimized. The approach is quite general in that it allows for any cost function and analysis tool.

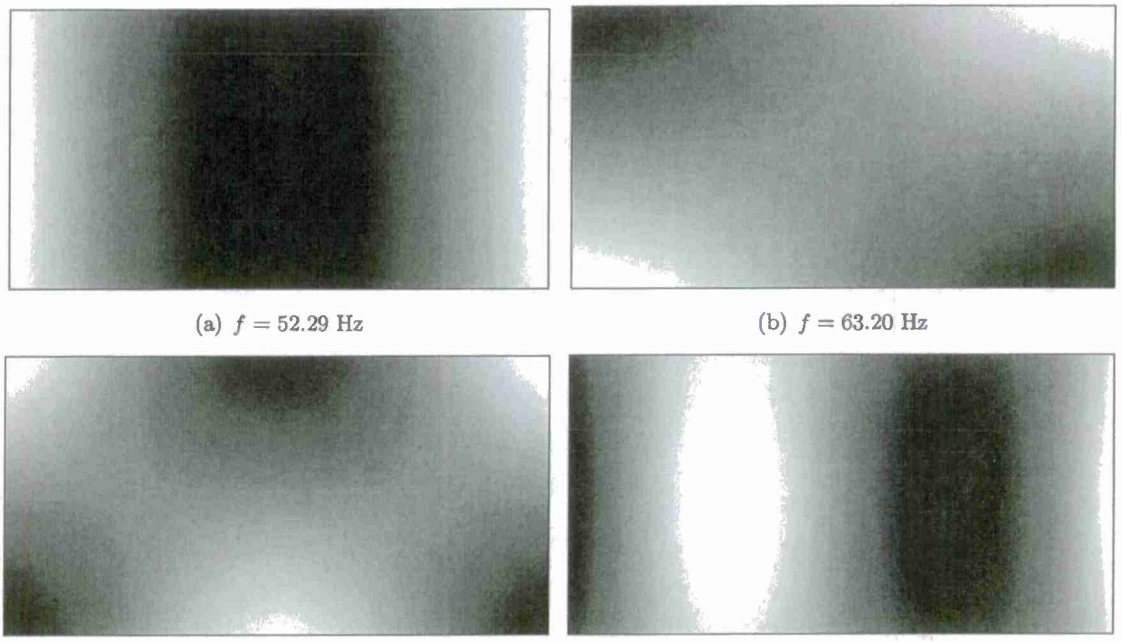

(a) $f = 52.29$ Hz (b) $f = 63.20$ Hz

(c) $f = 139.5$ Hz (d) $f = 145.2$ Hz

Figure 2.2: Four lowest non-rigid-body modes of an undamped, rectangular, aluminum plate.

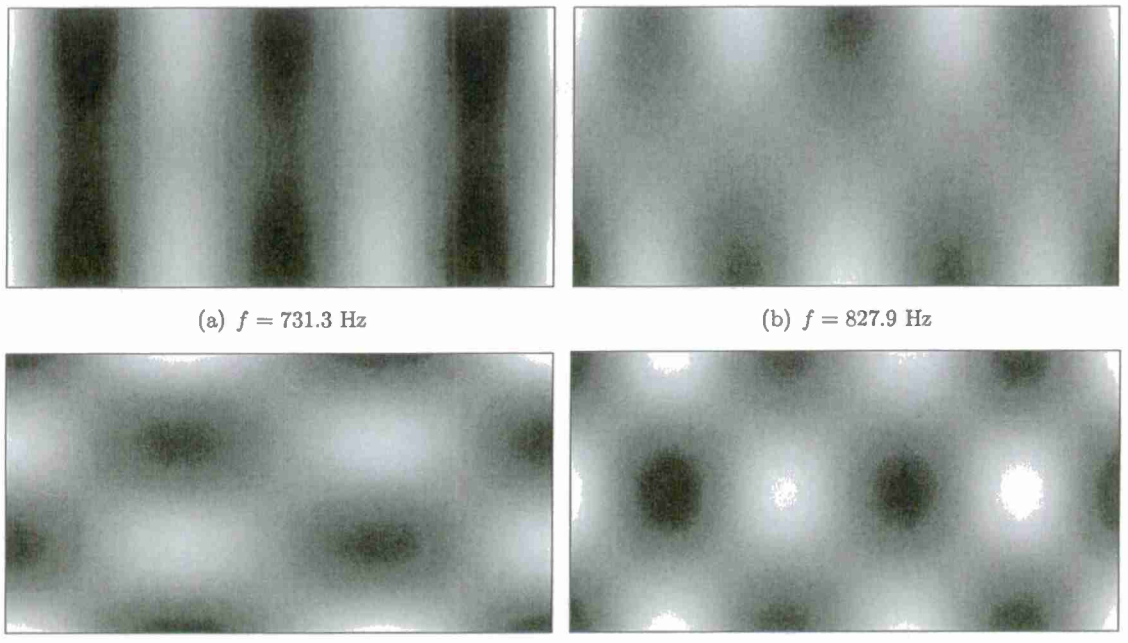

(a) $f = 731.3$ Hz (b) $f = 827.9$ Hz

(c) $f = 838.6$ Hz (d) $f = 845.7$ Hz

Figure 2.3: Four highest modes of an undamped, rectangular, aluminum plate less than 1000 Hz.

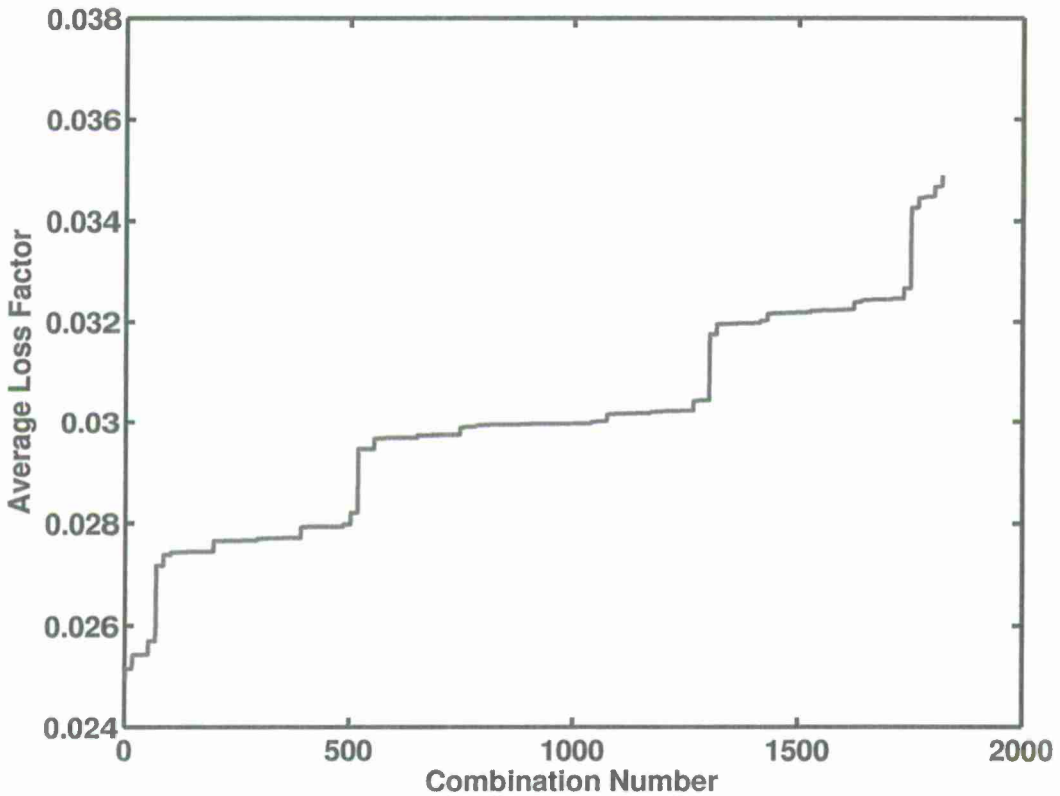


Figure 2.4: Plot of the average modal loss factor for natural frequencies less than 1000 Hz as a function of configuration number for 25% coverage.

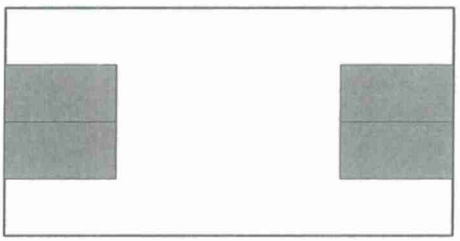

Figure 2.5: Locations of damping treatment for best average modal loss factor.

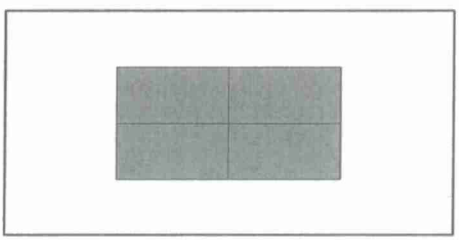

Figure 2.6: Locations of damping treatment for worst average modal loss factor.

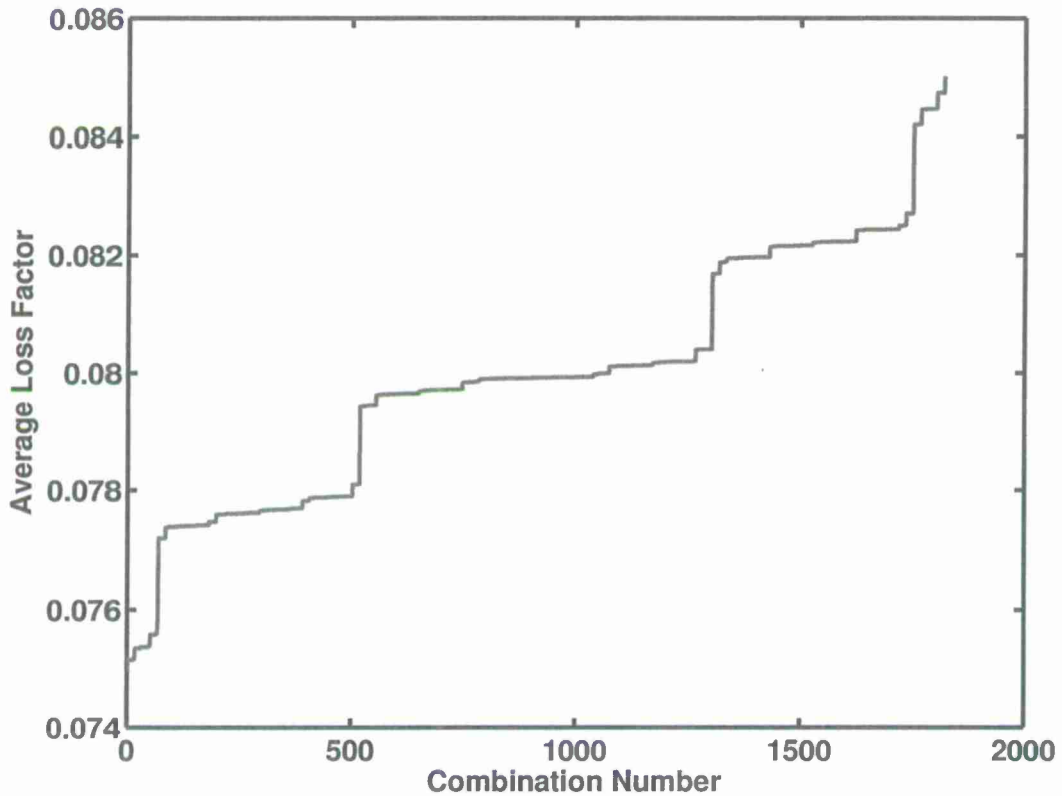


Figure 2.7: Plot of the average modal loss factor for natural frequencies less than 1000 Hz as a function of configuration number for 75% coverage.

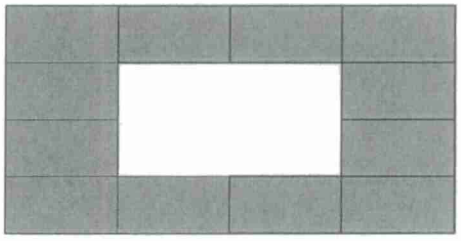

Figure 2.8: Locations of damping treatment for best average modal loss factor.

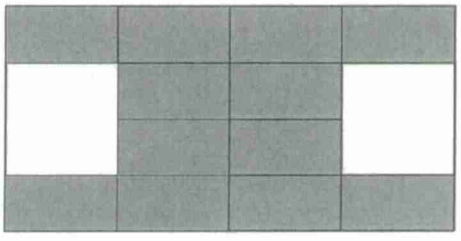

Figure 2.9: Locations of damping treatment for worst average modal loss factor.

# Chapter 3

# Optimizing the spatial distribution of damping in structures with boundary damping

## 3.1 Introduction

The present work seeks to optimize the spatial distribution of damping in structures with boundary damping. This work is motivated by design considerations, such as weight and cost, that often limit the amount of damping that can be used. In such cases, the designer must choose the spatial distribution of damping in order to reduce the structural vibration. One intuitively expects that the presence of boundary damping affects the optimal distribution of damping in the structure. In particular, one expects that the optimal design places damping treatments away from such boundaries in order to achieve an even distribution of power flow from the structure. To investigate this effect, finite element models of vibrating structures are developed in which the spatial distribution of damping is parameterized. These parameters are regarded as optimization parameters that are searched to minimize a cost function related to vibration or noise, such as the average response of the structure over a frequency band. Examples are presented that illustrate the effect of boundary damping on the optimal distribution of damping.

## 3.2 Literature Review

Optimizing the placement of damping on complex structures has received a modest amount of attention in the open literature. Perhaps the earliest work is from McQuillin and Kerwin [13, 14], which considered a simple example of a flexural wave on a beam or plate with patches of constrained layer and free layer damping. In this case, they were able to quantify a 'damping efficiency' parameter related to a damping patch. This parameter allowed the damping factor to be expressed as the product of a damping efficiency and a partial coverage ratio. Unfortunately, the details of that work do not appear to have been published in the open literature.

Much later, in 1997, Takewaki [15] took a more general approach in optimizing damper placements to reduce the sum of transfer function amplitudes. Dampers were generally assumed to be placed at each degree of freedom and the value of the dashpot constants were chosen as optimization

parameters. The cost function was chosen to be the sum of transfer function amplitudes evaluated at the undamped natural frequencies. In 2003, Sireteanu and Stoia [16] presented the optimization of a nonlinear damping treatment for vehicle suspension. The governing equations of motion were solved by a Newmark method and Monte Carlo simulation was used to explore the design space.

In 2005, Zheng *et al* [17] presented a very specific study on the layout optimization of damping treatments on a cylindrical shell. They used a genetic algorithm to find the optimal layout for reducing the structural volume displacement. Optimization parameters were chosen as the location and dimensions of each damping patch. They were able to reduce the structural volume displacement by more than 20 dB by applying partial coverage of a damping treatment to the shell. In 2007, Cimellaro [18] expanded the earlier work by Takewaki [15] by considering the simultaneous optimization of stiffness and damping in building structures with respect to acceleration, displacement, and base shear of a tall building structure.

In 2008, Arajo [19] *et al* presented an approach for optimizing laminated sandwich composite structures from finite element models. The authors proposed the Feasible Arc Interior Point Algorithm to maximize modal loss factors. One interesting feature of their work is the introduction of constraints on the optimization variables, which involved the static faliure criteria of the structure as well as the overall mass. The optimization parameters, referred to as "design variables" by the authors, were the viscoelastic core thickness, the constraining elastic face laminae thicknesses and orientation fiber angles.

The present work investigates the effect of boundary damping on the optimal placement of structural damping. In the following section, the modal strain energy method is used to understand how boundary damping affects the optimal placement of additional damping. Next, numerical simulations are presented that confirm the intuitive expectation that the optimal placement is away from highly damped boundaries.

## 3.3 Modal Perspective

Consider a discrete vibrating system with $N$ degrees of freedom. The Modal Strain Energy Method [20, 21, 22] conceptually divides a structure into an undamped portion and a damped portion, where the damped portion is assumed to be uniformly damped with a material loss factor $\eta_d$. One then defines the undamped eigenvalue problem,

$$\left(-\omega_n^2 \mathbf{M} + \mathbf{K}_u + \mathbf{K}_d\right) \boldsymbol{\phi}_n = \mathbf{0}, \tag{3.1}$$

where $\mathbf{K}_u$ and $\mathbf{K}_d$ are the real-valued undamped and damped stiffness matrices, respectively. The undamped eigenvectors are assumed orthonormal,

$$\boldsymbol{\phi}_n^T \mathbf{M} \boldsymbol{\phi}_n = 1. \tag{3.2}$$

The damped eigenvalue problem is

$$\left[-\Omega_n^2 (1 + i\eta_n)\mathbf{M} + \mathbf{K}_u + (1 + i\eta_d)\mathbf{K_d}\right] \boldsymbol{\psi}_n = \mathbf{0}, \tag{3.3}$$

where $\eta_n$ is the modal loss factor and $\eta_d$ is the material loss factor of the damped portion. Next, one approximates the damped eigenpair by the undamped eigenpair, so that

$$\Omega_n \approx \omega_n \tag{3.4}$$

$$\boldsymbol{\psi}_n \approx \boldsymbol{\phi}_n \tag{3.5}$$

Inserting these approximations into (3.3) and using (3.1) results in an approximation for the modal loss factor,

$$\eta_n \approx \eta_d \frac{\boldsymbol{\phi}_n^T \mathbf{K}_d \boldsymbol{\phi}_n}{\boldsymbol{\phi}_n^T \left(\mathbf{K}_d + \mathbf{K}_u\right) \boldsymbol{\phi}_n} \tag{3.6}$$

The fraction on the right-hand side is interpreted as the ratio of strain energy in the damped portion of the structure. Note that if all of the strain energy is in the damped portion of the structure, then the modal loss factor is the material loss factor. Using Eqn. 3.1,

$$\eta_n \approx \eta_d \frac{\boldsymbol{\phi}_n^T \mathbf{K}_d \boldsymbol{\phi}_n}{\omega_n^2} \tag{3.7}$$

Now consider a simple case in which the added damping occurs by the connection of a damped spring between a degree-of-freedom and ground. In this case, the damped stiffness matrix $\mathbf{K}_d$ is filled with zeros except for the $(a, a)$ element, where $a$ denotes the degree-of-freedom where the spring is attached. Further assuming that the undamped mode shapes are well-approximated by neglecting the damped stiffness, then

$$\left[-\omega_n^2 \mathbf{M} + \mathbf{K}_u\right] \boldsymbol{\phi}_n \approx \mathbf{0}. \tag{3.8}$$

This approximation allows one to conceptually move the damped spring to various locations on the structure while holding the undamped eigenvector and natural frequency constant. Equation 3.7 indicates that the modal loss factor would depend on the undamped eigenvector at the location of the damped spring,

$$\eta_n \approx \eta_d \frac{(\boldsymbol{\phi}_n)_a^2 \left(\mathbf{K}_d\right)_{aa}}{\omega_n^2} \tag{3.9}$$

At first glance, this result indicates that optimal placement of damping to maximize modal loss factor is independent of boundary location. Without additional assumptions, one cannot know whether the $a$th element of the undamped vector is smaller or larger near a boundary.

To explore the affect of a damped boundary, let the boundary be simply modeled by the connection of an additional damped spring between the $b$th degree-of-freedom and ground. Now the damped stiffness matrix has an additional nonzero element and Eqn. (3.9) becomes

$$\eta_n \approx \eta_d \frac{(\boldsymbol{\phi}_n)_a^2 \left(\mathbf{K}_d\right)_{aa} + (\boldsymbol{\phi}_n)_b^2 \left(\mathbf{K}_d\right)_{bb}}{\omega_n^2}. \tag{3.10}$$

Fixing the boundary location $b$ and varying the damping location $a$, it is seen that the optimal location is in general different from the optimal location found from (3.9). The addition of boundary damping has changed the optimal location for added damping. This observation may be extended by optimizing the location of damping by minimizing the average of many loss factors. It may also by extending by considering added damping and boundary damping that involves more than one degree-of-freedom.

## 3.4 Numerical Simulations

In order to investigate the intuitive expectation that optimal damping placement is away from highly damped boundaries, numerical examples are presented here for the case of a serial chain of

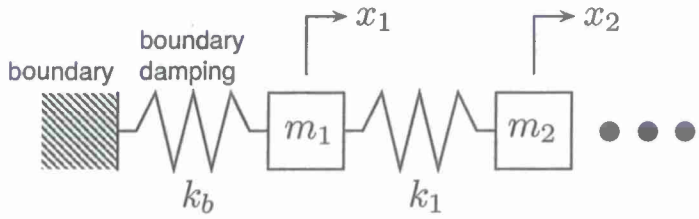


Figure 3.1: Drawing of a portion of the ten degree-of-freedom system. The chain extends to the right until the tenth mass is connected to ground by a boundary damping spring, $k_b$, similar to the left-hand side.

oscillators. A schematic of a portion of the system is shown in Figure 3.1. Ten masses are connected in a chain by nine springs, which shall be referred to here as interior springs. The masses are chosen to be 1 kg each and the springs are random with a uniform distribution of spring constants over the interval $[0, 1]$ N/m.

Boundary springs with material loss factors of $\eta = 1$ connect the end masses, corresponding to degrees-of-freedom 1 and 10, to ground with a spring constant of 1 N/m. Damping is added by adding three damped springs to three of the ten masses. Each of the damped springs connect a mass to ground and have a spring constant of 1 N/m and a loss factor of $\eta = 0.1$. All combinations of ten masses are chosen three at a time, yielding a total of 120 combinations. For each realization, the complex eigenvalues are found numerically, without the approximation of the Modal Strain Energy Method. The best combination is the combination with the highest modal loss factor. Several realizations are analyzed and the results are shown in Figure 3.2. Each circle in the plot represents the optimal placement of added damping, so that a horizontal strip corresponds to an optimal combination of damping for a fixed realization. Note that the optimal combinations are not uniformly distributed but appear to be more concentrated in the middle, away from the boundary damping at the left and right hand sides of the plot.

To investigate this effect further, Fig. 3.3 corresponds to the case where the boundary damping at degree-of-freedom 10 (right-hand side of the figure) was removed. This produced an obvious shift of the interior damping to the right-hand side of the figure, apparently compensating for the lack of damping in this portion of the model. In all realizations, one of the three locations is chosen as the far right-hand side where there is no boundary damping. As a final check, the boundary damping was removed at both ends and the resulting optimal combinations are shown in Figure 3.4. In this figure, the optimal damping combinations are more uniformly spread across the degrees-of-freedom.

## 3.5 Conclusions

In conclusion, this work presented analytical approximations that indicate the importance of boundary damping when trying to find optimal placement of damping. Numerical simulations, in which the connecting springs of a ten degree-of-freedom system were randomly varied, further revealed that the optimal placement of damping depends critically on boundary damping.

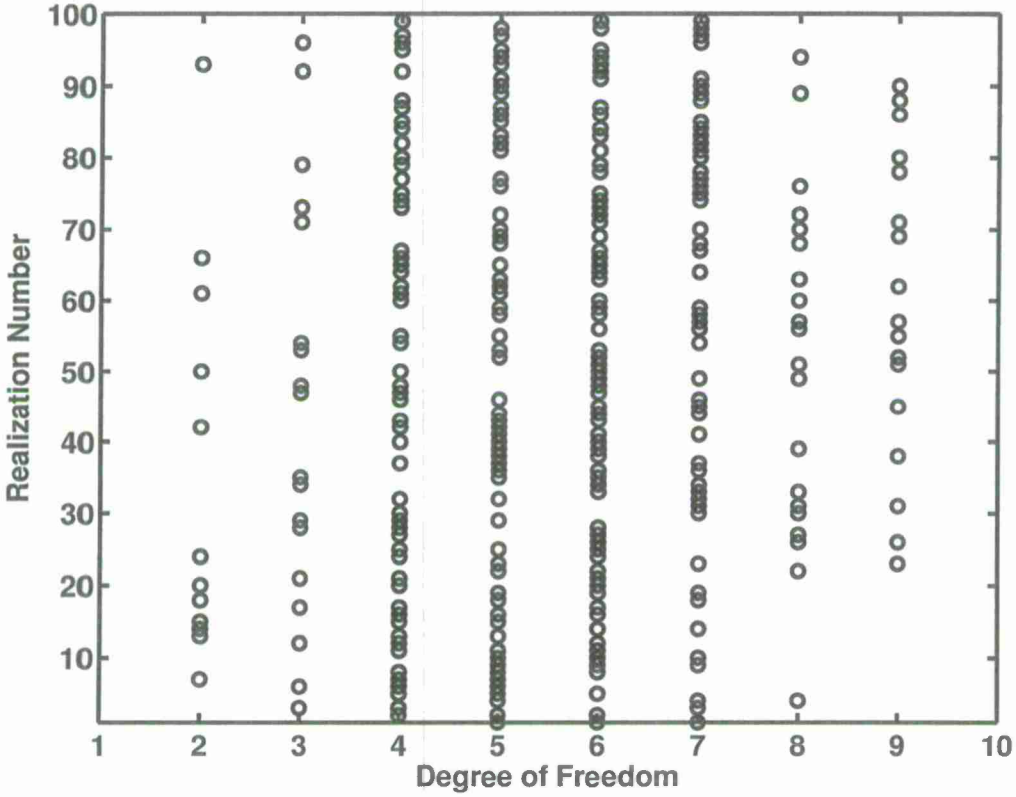


Figure 3.2: Combinations of optimal damping placement for boundary loss factor $\eta = 1$ on each side and added damping $\eta = 0.1$ at three locations.

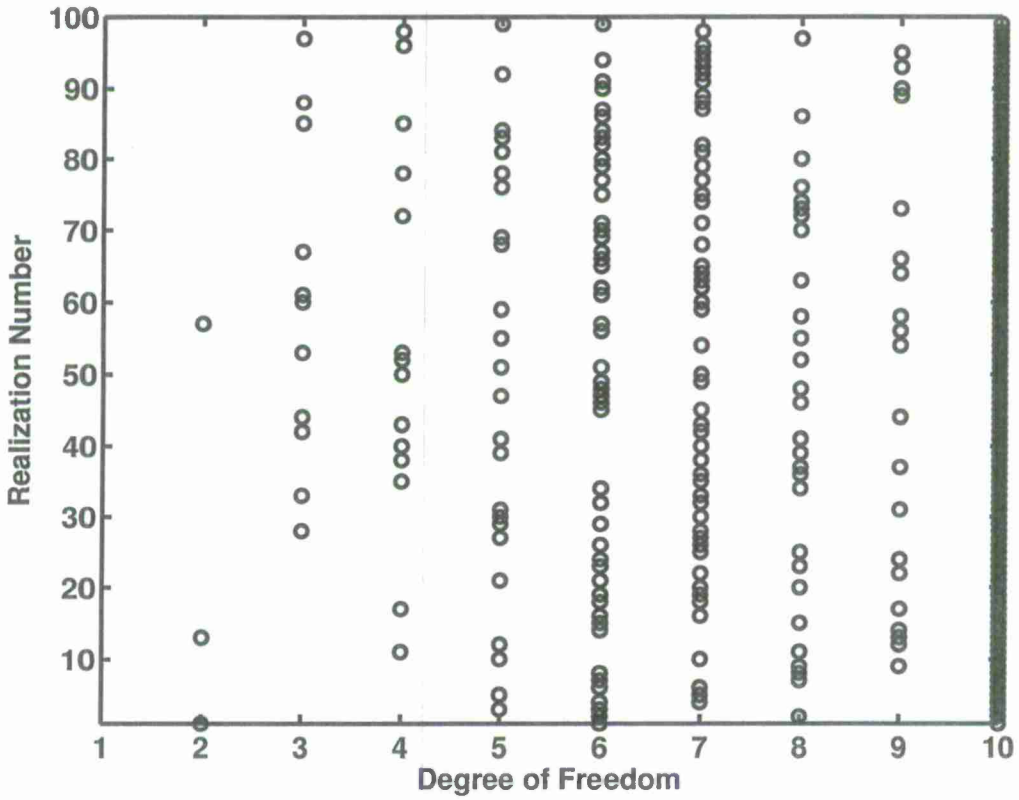


Figure 3.3: Combinations of optimal damping placement for boundary loss factor $\eta = 1$ on only the left-hand side and added damping $\eta = 0.1$ at three locations.

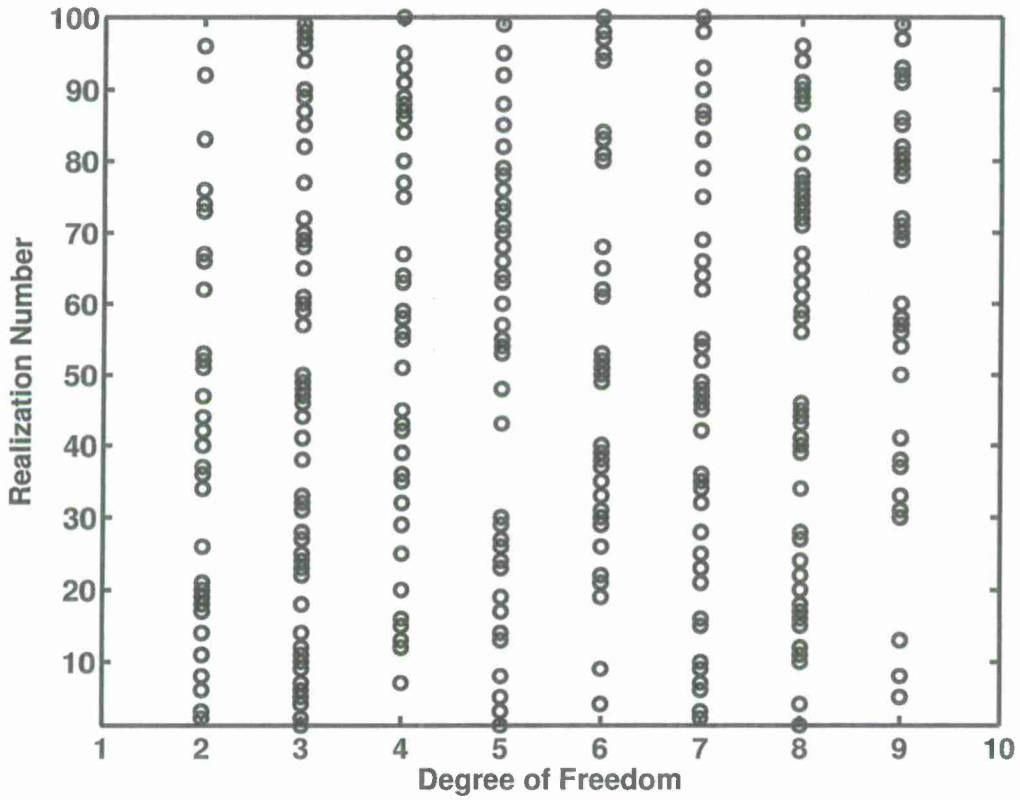


Figure 3.4: Combinations of optimal damping placement for no boundary damping and added damping $\eta = 0.1$ at three locations.

# Chapter 4

# The use of thermal imaging techniques for evaluation of constrained layer treatments for vibrational damping

## 4.1 Introduction

Constrained layer damping (CLD) treatment systems are widely used in complex structures to dissipate vibrational energy. In many applications it is important to understand the relative effectiveness between different treatments. Unfortunately, a viable technique for determining this effectiveness has yet to be developed.

This work develops the theoretical basis for determining the effectiveness of CLD treatments using thermal imaging technology. Heat generation in CLD treatments is predicted and the associated temperature distribution is modeled in time and space. The effect of materials choice and excitation scheme on temperature rise is discussed. With a temperature resolution of 0.025°C, thermal imaging is presented as a potential in-situ technique for mapping these temperature changes in real systems and from this, developing an expression for damping effectiveness.

Constrained layer damping (CLD) treatments consist of a base layer, or the structure to be damped, a viscoelastic layer and a constraining layer. All three layers are adhered together, with the viscoelastic layer sandwiched between the base and the constraining layer. When exposed to vibration, the viscoelastic layer is strained in a shear mode. The amount of energy removed from the vibrating system is proportional to the rate of viscoelastic shear. Because of internal friction mechanisms, this shear rate energy is converted to heat and conducted through the system.

This work attempts to map the heat generation in CLD treatments to gain insight into their effectiveness, or relative ability to remove vibrational power from a complex system. This technique is framed in the context of thermal imaging, which allows temperature changes on the surface of solids to be mapped both spatially and temporally where this temperature rise occurs as a function of heat generation within the CLD. Recent literature[23, 24] in the field of thermography has placed the limit of temperature sensitivity on thermal cameras at 0.025°C. Recent literature[25] investigating the temperature rise in solids while exposed to cyclic stress or vibration environments

has shown that temperature changes in excess of 1°C can be achieved. These facts give confidence to the potential for detecting a temperature rise in viscoelastic solids by means of a thermal camera. This work attempts to not only show the viability of this technique but also explain how the effectiveness of a CLD treatment can be tied into it.

## 4.2 Motivation

Understanding the effectiveness of damping becomes important for different reasons in different industries. In maritime applications, damping treatments are replaced regularly, leading to increased costs when ineffective damping treatments are replaced. In aircraft and spacecraft structures, ineffective damping leads to unnecessary weight and thus lower allowances for payload and critical systems. Understanding the effectiveness of individual damping treatments could lead to lower costs, complexity and system mass in many commercial applications. Unfortunately, with structures continuously growing in complexity and size, determining how effective or ineffective damping treatments are has becoming increasingly difficult. Analytical schemes become nearly impossible to undertake and numerical schemes have difficulty in modeling every mass, damping and stiffness element within a real structure thus leading to inaccuracies. This leaves experimental and in-situ techniques. The proposed technique would not only give insight to the power dissipation characteristics of the structural system but is also an in-situ, no destructive testing technique - ideal for the applications discussed previously.

## 4.3 Literature review

The literature upon which this work is based falls into two general categories. These are constrained layer damping (CLD) treatment theory and temperature profiling techniques. As such this literature review is broken into sections representative of each of these topics.

### 4.3.1 CLD Theory

The first major developments and the basis for most CLD treatment theory was put forth by E.M. Kerwin[26]. His seminal paper explored the damping of sandwich beams in which a viscoelastic layer was adhered between two perfectly elastic layers. This paper made many basic assumptions allowing for a simple analysis, including:

1. Considering the beam to be either infinitely long or to be simply supported in its boundary conditions while vibrating at a natural frequency
2. Disallowing slip between adjoining layers in the structure
3. Elastic plate layers displace transversely by the same amount

Kerwin [26] showed that the most important mechanism in power dissipation by sandwich beams was shear deformation of the viscoelastic layer. His method employed the use of a complex valued bending stiffness dependent on a loss factor, $\eta$. This loss factor introduced material loss, due to the viscoelastic layer, into the equations of motion for a sandwich beam. This technique stems from the Kelvin-Voigt model of viscoelastic solids where the elastic modulus is observed to vary with the strain and strain rate of the viscoelastic material. When the strain is sinusoidal, as in

vibration theory, the strain rate introduces the complex $i$, leading to a complex valued elastic and shear modulus and eventually a complex valued bending stiffness.

Later, DiTaranto [27] furthered this work by developing a sixth order equation of motion for the response of sandwich beams. This formulation allowed for the analysis of sandwich beam structures of finite length and arbitrary end conditions. As it was a sixth order differential equation of motion, six boundary conditions were needed for its solution. Aside from the typical four conditions found for a solid beam (two conditions on each end) one more condition for each of the ends was needed to define longitudinal constraints and satisfy the sixth order equation.

While these two papers paved the way for sandwich beam analysis, concurrently, researchers were applying sandwich beam theory to thin plate sandwich structures. Ross, Kerwin and Ungar [28] were the first to produce this theory. The structures consisted of an elastic base plate, a viscoelastic core and and elastic constraining layer, similar to the sandwich beam. This system is strongly representative of real CLD treatment systems and as such a proper analysis of it can produce response functions that are extremely close to those of a real CLD treatment system. Many researchers [29, 30, 31] have been involved in the development of this thin sandwich plate theory.

One of the most accurate theories to date is the analysis put forth by Rao and Nakra [29]. In their work, the response of unsymmetrical, sandwich beams and plates was developed given a small number of assumptions. For their unsymmetrical plate theory, the assumptions they made follow[29].

1. Extensional effects within the viscoelastic material are ignored.
2. All plane transverse sections of the elastic layers remain plane and normal to the longitudinal fibers of the plate layers after bending.
3. The transverse displacement remains constant throughout the thickness of the plate.
4. There is perfect continuity of displacement at the interfaces.
5. All displacements are considered small.

The only assumption here that may be troubling is the discarding of viscoelastic extensional effects. Fortunately, in most cases, shear deformation provides a much stronger power dissipation mechanism than that of extension in the viscoelastic cores of CLD treatments[32, 28, 33]. The strength of this formulation comes in its accounting for inertia effects. Using a variational method, Rao and Nakra were able to account for rotary and longitudinal inertia as opposed to the majority of research which focused only on transverse inertia[27, 30, 31, 28]. In doing so a higher order approximation for the equations of motion of sandwich plates was established.

Since the work of Rao and Nakra [29], most sandwich plate vibration theory has focused on the finite element technique as applied to sandwich plate structures (see [34],[35]), the analytical and numerical solutions to the response of sandwich plate structures with fiber composite base and constraining layers (see [36],[37]) as well as the response of sandwich structures more exotic than beams and plates. As the work to follow only requires a basis of comparison for plate structures, these developments are not detailed and the primary work on which the analysis is based is that of Rao and Nakra [29].

### 4.3.2 Temperature Profiling

Within this work, temperature profiling refers to the establishment of temperature distributions through structures as well as their temporal characteristics. Approaches fall into two general categories: experimental and theoretical techniques. Experimentally, this work focuses on thermal imaging technology and its capabilities while theoretically this work focuses on the framework and solutions required to describe simplified systems using the heat diffusion equation.

The heat diffusion equation, which describes the temperature of a body and its changes in time and space is a partial differential equation and, in principle, difficult to solve when non-homogeneous. One of the central models of this work is a system of non-homogeneous heat diffusion equations stemming from a heat production term within the CLD viscoelastic layer. Carslaw and Jaegar [38] published solutions to similar systems of equations in their comprehensive work on heat conduction in solids. While vast amounts of research has been conducted in the field of heat diffusion and conduction in the years since this work, Carslaw and Jaegar [38] provided the necessary framework for analyzing the temperature distribution through CLD systems.

The use of thermal imaging cameras is not foreign to the field of modal and vibrational analysis. E.G. Henneke et.al. [39] coined the term "vibrothermography" to describe a non-destructive technique for evaluating damage in structures. From the abstract of this paper,

> Vibrothermography is an NDE technique whereby a structure is excited with mechanical vibrations and the temperature profile on the surface is mapped by real-time video thermography. Damage in the structure is frequently more efficient at converting the input mechanical energy to heat than are undamaged regions of the structure. Hence damage appears on the thermal map as warmer regions.

Since this work, a number of researchers have developed the field of vibrothermography[40, 41, 23, 39]. While vibrothermography does not apply directly to the development of CLD temperature distributions, its results do. Specifically the results for the work of Audenino et. al.[24]. Here, Audenino, et. al., were able to generate large temperature changes in small prepared samples of a number of metals. Using a cyclical stress with a magnitude that neared the elastic limit of the sample, temperature changes on the order of 100°C were noted. This temperature is well within the range of thermal imaging cameras at a stress magnitude within the material's linear elastic regime. Audenino et. al. [42] also made use of a thermal imaging system with a temperature resolution of 0.025°C. The availability of cameras with this sort of resolution would allow for even the smallest of temperature changes within a CLD treatment to be detected and quantified. These figures not only provided confidence in the abilities of thermal imaging but also provided a motivation for this work.

Outside of the developments of vibrothermography, research in the field of civil engineering has led the characterization of temperature rise in viscoelastic damping materials. Lai et. al. [25], developed an expression for the temperature rise in a viscoelastic material using a representation of shear stress integrated over time assuming no heat conduction to a host structure. The purpose of this work was to predict the effect of temperature rise on the properties of viscoelastic materials at high shear strain levels (˜125%). Their results, along with the finite element results utilizing a similar analysis which included heat conduction and convection in the work of Lai et. al. [43], predicted temperature rises on the order 1-2°C within viscoelastic materials undergoing what they considered 'small deflection' excitation.

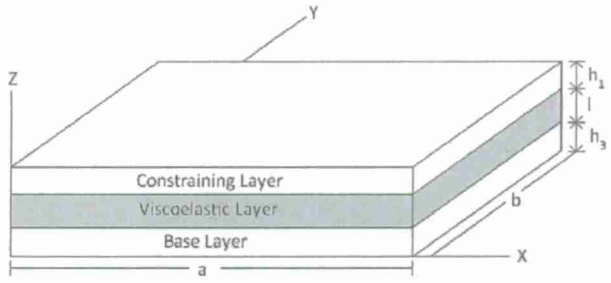


Figure 4.1: A typical sandwich plate system. Coordinate systems and length scales are noted. Constraining layer, viscoelastic layer and base layer pertain to the nomenclature used through CLD treatment theory.

## 4.4 Constrained Layer Damping Analysis

Formulation

The primary goal of constrained layer damping analysis as pertaining to this work is in establishing the power dissipated by the viscoelastic layer of a sandwich plate system. A typical sandwich plate system, and the one referenced throughout this work, can be seen in Figure 4.1. In order to establish its power dissipation, first the response characteristics of the system must be understood.

The following formulation of constrained layer damping treatment response primarily follows the work of Rao and Nakra[29]. This work resulted in a series of equations of motion for unsymmetrical sandwich plate structures. In accounting for shear deformation as well as rotary, transverse and longitudinal inertia effects and allowing for arbitrary boundary conditions, this work provides an accurate analytical formulation for CLD systems. The equations of motion they developed are,

$$\begin{aligned} 0 &= \gamma_1 \left\{ u_1'' + \frac{(1+\nu_1)}{2} v_1'^{*} + \frac{(1-v_1)}{2} u_1^{**} \right\} + \gamma_2 \left\{ \frac{c}{h_2^2} w' - \frac{(u_1 - u_3)}{h_2^2} \right\} - \\ &\quad \rho_1 h_1 \ddot{u}_1 - \rho_2 L \left( \frac{\ddot{u}_1}{3} + \frac{\ddot{u}_3}{6} + \ddot{w}' \varepsilon_3 \right) \end{aligned} \tag{4.1}$$

$$\begin{aligned} 0 &= \gamma_1 \left\{ v_1^{**} + \frac{(1+\nu_1)}{2} u_1'^{*} + \frac{(1-v_1)}{2} v_1'' \right\} + \gamma_2 \left\{ \frac{c}{h_2^2} w^* - \frac{(v_1 - v_3)}{h_2^2} \right\} - \\ &\quad \rho_1 h_1 \ddot{v}_1 - \rho_2 L \left( \frac{\ddot{v}_1}{3} + \frac{\ddot{v}_3}{6} + \ddot{w}^* \varepsilon_3 \right) \end{aligned} \tag{4.2}$$

$$\begin{aligned} 0 &= \gamma_3 \left\{ u_3'' + \frac{(1+\nu_3)}{2} v_3'^{*} + \frac{(1-\nu_3)}{2} u_3^{**} \right\} - \gamma_2 \left\{ \frac{c}{h_2^2} w' - \frac{(u_1 - u_3)}{h_2^2} \right\} - \\ &\quad \rho_3 h_3 \ddot{u}_3 - \rho_2 L \left( \frac{\ddot{u}_1}{6} + \frac{\ddot{u}_3}{3} + \ddot{w}' \varepsilon_4 \right) \end{aligned} \tag{4.3}$$

$$0 = \gamma_3 \left\{ v_3^{**} + \frac{(1+\nu_3)}{2} u_3^{'*} + \frac{(1-\nu_3)}{2} v_3^{''} \right\} - \gamma_2 \left\{ \frac{c}{h_2^2} w^* - \frac{(v_1 - v_3)}{h_2^2} \right\} - \rho_3 h_3 \ddot{v}_3 - \rho_2 L \left( \frac{\ddot{v}_1}{6} + \frac{\ddot{v}_3}{3} + \ddot{w}^* \varepsilon_4 \right) \tag{4.4}$$

$$0 = (D_1 + D_3)\nabla^4 w - \gamma_2 \frac{c}{t_2^2} \left\{ c \left( w'' + w^{**} \right) - \right.$$
$$\left. -u_1' + u_3' - v_1^* + v_3^* \right\} - \frac{\rho_1 h_1^3 + \rho_3 h_3^3}{12} \left( w'' + w^{**} \right) -$$
$$\rho_2 L \left\{ \varepsilon_3 \left( u_1' + v_1^* \right) + \varepsilon_4 \left( u_3' + v_3^* \right) + \left( \varepsilon_1^2 + \frac{\varepsilon_2^2}{12} \right) \left( w'' + w^{**} \right) \right\} +$$
$$\rho \ddot{w} + Q(x,y) g(t) \tag{4.5}$$

where the bending stiffness of the elastic plates is,

$$D_i = \frac{E_i h_i^3}{12 \left(1 - \nu_i^2\right)} \; i = 1, 3,$$

and,

$$\gamma_i = \frac{E_i h_i}{1 - \nu_i^2} \; i = 1, 3,$$

$$c = L + \left( \frac{h_1 + h_3}{2} \right)$$

$$\gamma_2 = G^* L,$$

$$\varepsilon_1 = \tfrac{h_3 - h_1}{4},\ \varepsilon_2 = \tfrac{h_1 + h_3}{2},\ \varepsilon_3 = \tfrac{h_3 - 2h_1}{12},\ \varepsilon_4 = \tfrac{2h_3 - h_1}{12},$$

and subscript 1 refers to the base plate, subscript 2 refers to the viscoelastic layer and subscript 3 refers to the constraining plate.

These equations of motion can be used to establish the response of a plate with arbitrary boundary conditions. However, for simplicity's sake, we wil assume the plate is simpy supported on all sides. The generalized forcing function can be written as,

$$Q(x,y)g(t) = \sum_{m=1}^{\infty} \sum_{n=1}^{\infty} Q_{mn} \sin \frac{m\pi x}{a} \sin \frac{n\pi y}{b} \sin \omega t \tag{4.6}$$

where the longitudinal, latitudinal and transverse displacements follow as,

$$\left\{ \begin{array}{c} u_1 \\ u_3 \end{array} \right\} = \sum_{m=1}^{\infty} \sum_{n=1}^{\infty} \left\{ \begin{array}{c} U_{1mn} \\ U_{3mn} \end{array} \right\} \cos \frac{m\pi x}{a} \sin \frac{n\pi y}{b} \sin \omega t, \tag{4.7}$$

$$\left\{ \begin{array}{c} v_1 \\ v_3 \end{array} \right\} = \sum_{m=1}^{\infty} \sum_{n=1}^{\infty} \left\{ \begin{array}{c} V_{1mn} \\ V_{3mn} \end{array} \right\} \sin \frac{m\pi x}{a} \cos \frac{n\pi y}{b} \sin \omega t, \tag{4.8}$$

$$w = \sum_{m=1}^{\infty}\sum_{n=1}^{\infty} W_{mn} \sin\frac{m\pi x}{a} \sin\frac{n\pi y}{b} \sin\omega t, \tag{4.9}$$

Given these conditions and the assumptions made previously, the solutions to the equations of motion (equations 4.1 through 4.5) for the sandwich plate have been solved as detailed in the work of Rao and Nakra [29]. The form of the response used here follows that of Sun et. al. [32].

Solution of the equations of motion is achieved by inserting the Fourier series representations of the displacements into equations 4.1 through 4.5, and solving the system of equations that develops for the complex magnitudes of displacement. This system of equations is,

$$\begin{bmatrix} d_2^R + id_2^I & d_4 & -d_3^R - id_2^I & 0 & -d_1^R - id_1^I \\ d_4 & e_2^R + id_2^I & 0 & -d_3^R - id_2^I & -e_1^R - ie_1^I \\ -d_3^R - id_2^I & 0 & f_2^R + id_2^I & f_3^R & -f_1^R + id_1^I \\ 0 & d_3^R - id_2^I & f_3^R & g_2^R + id_2^I & -g_1^R - ig_1^I \\ -d_1^R - id_1^I & -e_1^R - ie_1^I & -f_1^R + id_1^I & -g_1^R - ig_1^I & -h_1^R - ih_1^I \end{bmatrix} \begin{bmatrix} U_{1mn} \\ U_{3mn} \\ V_{1mn} \\ V_{3mn} \\ W_{mn} \end{bmatrix} = \begin{bmatrix} 0 \\ 0 \\ 0 \\ 0 \\ Q_{mn} \end{bmatrix} \tag{4.10}$$

Assuming the plate is forced at its center with a harmonic force, the values of the coefficients are,

$$Q_{mn} = \frac{4F_0 \sin\frac{m\pi}{2} \sin\frac{n\pi}{2}}{bm\pi E_3}, \tag{4.11}$$

$$d_1^I = \delta_{2,3}\left(1 + \frac{1+\theta_{1,3}}{2\theta_{2,3}}\right)\eta, \tag{4.12}$$

$$d_1^R = \delta_{2,3}\left(1 + \frac{1+\theta_{1,3}}{2\theta_{2,3}}\right) + \frac{\lambda\xi_{2,3}}{12}\frac{\theta_{2,3}}{\xi_{1,3}}\left(1 - 2\theta_{1,3}\right), \tag{4.13}$$

$$d_4 = \frac{\varphi_{1,3}\theta_{1,3}\beta n\xi}{2(1-\psi_{1,3}\nu_3)}, \tag{4.14}$$

$$d_2^I = \frac{\delta_{2,3}}{\theta_{2,3}\beta m}\eta, \tag{4.15}$$

$$d_2^R = \frac{\varphi_{1,3}\theta_{1,3}}{1-\nu_1^2}\left\{m\beta + \frac{1-\nu_1}{2}\xi^2\beta^2\frac{n^2}{\beta m}\right\} + \frac{\delta_{2,3}}{\theta_{2,3}\beta m} - \frac{\lambda}{\beta m}\theta_{1,3} - \frac{\lambda}{\beta m}\frac{\xi_{2,3}}{\xi_{1,3}}\frac{\theta_{2,3}}{3}, \tag{4.16}$$

$$d_3^R = \frac{1}{\beta m}\left(\frac{\delta_{2,3}}{\theta_{2,3}} + \lambda\frac{\xi_{2,3}}{\xi_{1,3}}\frac{\theta_{2,3}}{6}\right), \tag{4.17}$$

$$e_1^I = \frac{n}{m}\xi d_1^I, \tag{4.18}$$

$$e_1^R = \frac{n}{m}\xi d_1^R, \tag{4.19}$$

$$e_2^R = \frac{\varphi_{1,3}\theta_{1,3}}{1-\psi_{1,3}^2\nu_3^2}\left\{\frac{n^2}{m}\xi^2\beta + \frac{1}{2}(1-\psi_{1,3}\nu_{1,3})\beta m\right\} + \frac{\delta_{2,3}}{\theta_{2,3}\beta m} - \frac{\lambda}{\beta m}\left(\theta_{1,3} + \frac{\xi_{2,3}}{\xi_{1,3}}\frac{\theta_{2,3}}{3}\right), \tag{4.20}$$

$$f_1^R = \frac{\lambda\xi_{2,3}}{\xi_{1,3}}\frac{\theta_{2,3}}{12}(2-\theta_{1,3}) - \delta_{2,3}\left(1+\frac{1+\theta_{1,3}}{2\theta_{2,3}}\right), \tag{4.21}$$

$$f_2^R = \frac{1}{1-\nu_3^2}\left(m\beta + \frac{1-\nu_3}{2}\xi^2\beta\frac{n^2}{m}\right) + \frac{\delta_{2,3}}{\theta_{2,3}\beta m} - \frac{\lambda}{\beta m}\left(\frac{1}{\xi_{1,3}} + \frac{\theta_{2,3}\xi_{2,3}}{3\xi_{1,3}}\right), \tag{4.22}$$

$$f_3^R = \frac{n\beta\xi}{2\left(1-\nu_3\right)}, \tag{4.23}$$

$$g_1^I = \frac{n}{m}\xi f_1^I, \tag{4.24}$$

$$g_1^R = \frac{n}{m}\xi f_1^R, \tag{4.25}$$

$$g_2^R = \frac{1}{1-\nu_3^2}\left(\frac{n^2}{m}\beta\xi^2 + \frac{1-\nu_3}{2}m\beta\right) + \frac{\delta_{2,3}}{\theta_{2,3}\beta m} - \frac{\lambda}{\xi_{1,3}\beta m} - \frac{\lambda}{3}\frac{\xi_{2,3}}{\xi_{1,3}}\frac{\theta_{2,3}}{\beta m}, \tag{4.26}$$

$$h_1^I = m\beta\left(1+\frac{n^2}{m^2}\xi^2\right)\left\{1+\frac{1+\theta_{1,3}}{2\theta_{2,3}}\right\}^2\delta_{2,3}\eta\theta_{2,3}, \tag{4.27}$$

$$\begin{aligned} h_1^R \;=\; & m^2\beta^2\left[\left\{\frac{\varphi_{1,3}\theta_{1,3}^3}{12(1-\psi_{1,3}^2\nu_3^2} + \frac{1}{12(1-\nu_3^2)}\right\}\left\{1+2\xi^2\frac{n^2}{m^2}+\frac{n^4}{m^4}\xi^4\right\}\right. \\ & \left.+\frac{\theta_{2,3}}{\beta^2m^2}\left(1+\frac{n^2\xi}{m^2}\right)\left(1+\frac{1+\theta_{1,3}}{2\theta_{2,3}}\right)^2\delta_{2,3}\right] \\ & -\lambda\left[\frac{m\beta}{12}\left(1+\frac{n^2\xi^2}{m^2}\right)\left\{\theta_{1,3}^3+\frac{1}{\xi_{1,3}}+\frac{\xi_{2,3}}{\xi_{1,3}}\theta_{2,3}\left(1+\theta_{1,3}^2-\theta_{1,3}\right)\right\}\right. \\ & \left.+\frac{1}{m\beta}\left(\theta_{1,3}+\frac{1}{\xi_{1,3}}+\frac{\xi_{2,3}}{\xi_{1,3}}\theta_{2,3}\right)\right] \end{aligned} \tag{4.28}$$

where,

$$\lambda = \frac{\rho_1\omega^2h_3^2}{E_3},$$

the non-dimensional Poisson's ratio for the two eastic plates is,

$$\psi_{1,3} = \frac{\nu_1}{\nu_3},$$

the non-dimensional ratio of layer thickness is,

$$\theta_{i,j} = \frac{h_i}{h_j}$$

with $h_2 = l$. The ratio of layer densities is,

$$\xi_{i,j} = \frac{\rho_i}{\rho_j},$$

Also,

$$\delta_{2,3} = \frac{G}{E_3},$$

the ratio of side lengths of the plate is,

$$\xi = \frac{a}{b},$$

the ratio of elastic moduli of the elastic plates is,

$$\varphi_{1,3} = \frac{E_1}{E_3},$$

and,

$$\beta = \frac{\pi h_3}{a}.$$

Once this set of equations is solved, expressions for the response of the plate are easily found. For this analysis, the main concern is the transverse displacement response of the plate. This is due to the fact that in finding an expression for the power input to the system, only the transverse component of displacement is used. This is discussed later.

The first concern in using these equations is determining whether or not the plate is vibrating within a linear elastic regime. In order to determine this, some constraint must be placed on the response. Since these equations assume that the plate is undergoing small amplitude vibrations it is difficult to determine when the response moves from linear to non-linear. This is generally accomplished by studying the transfer function of the response and increasing the forcing function magnitude until the transfer function changes. This indicates that the response no longer varies linearly with the input force. Since these equations assume linearity, the transfer function does not change no matter how large the magnitude of the input force. Therefore an approximate constraint must be established. There are two general methods for doing this: (1) require that the maximum strain in the plate remains below a specified level or (2) require that the ratio of maximum transverse displacement in the plate to a characteristic length in the plate remains below a specified level. Here, linear elastic vibrations are defined to occur when the ratio of maximum transverse displacement to the total thickness of the sandwich plate is equal to or less than 0.01. Mathematically this means the response of the plate is linear when,

$$w_{MAX} \leq 0.01(h_1 + l + h_3). \tag{4.29}$$

Constraining the transverse displacement as opposed to the plate strain to determine the linear elastic limit was chosen because of its simplicity to find a limit. Given the compliance transfer function (displacement/force) of the plate, $H_{comp}(\omega)$, the input force which elicits the maximum linear elastic response of the sandwich plate, $F_{0,MAX}$, is found as a function of excitation frequency by,

$$F_{0,MAX} = \frac{0.01(h_1 + l + h_3)}{H_{comp}(\omega)}. \tag{4.30}$$

Now with an understanding of the level to which a structure can be forced and its response thereby predicted by equations 4.11 through 4.28, the power dissipated by the structure can be calculated.

First, the power input to the system by the force is easily determined. Given that the input is harmonic, the complex amplitude of transverse velocity at any point can be determined by,

$$V = i\omega w. \tag{4.31}$$

Here, the response and input at any location is temporally dependent on a sinusoid(see equations 4.6 and 4.9). In this case, phase information is contained within the complex amplitude of the response. Using these amplitudes, the power transferred to the plate by the excitation system is,

$$P_{in}(\omega) = \frac{1}{2}\mathrm{Re}\{F_0(\omega) \cdot V^*(\omega)\} \tag{4.32}$$

where the star denotes the complex conjugate. Using the formulation established previously, this can also be written as,

$$P_{in}(\omega) = \frac{1}{2}\mathrm{Re}\left\{F_0(\omega) \cdot \left\{i\omega \sum_n^\infty \sum_m^\infty W_{mn}(\omega) \sin\left(\frac{n\pi x}{a}\right) \sin\left(\frac{m\pi y}{b}\right)\right\}^*\right\} \tag{4.33}$$

Now assuming that the plate is vibrating at steady state,

$$P_{in} = P_{out} + P_{dis}, \tag{4.34}$$

for this system. We also know that the power out term is equal to zero. At the plate boundaries a force may develop but the velocity for a simple support is always equal to zero by definition. Without a velocity at its edges, power has no way to transfer out of the sandwich plate. Therefore, all power in must be equal to power dissipated. Normalizing for volume of damping material the power dissipated by the damping material per unit volume, $A_0$, is,

$$A_0 = \frac{P_{in}(\omega)}{l \cdot a \cdot b}. \tag{4.35}$$

This is the only term from CLD theory that plays a role in the temperature distribution equations.

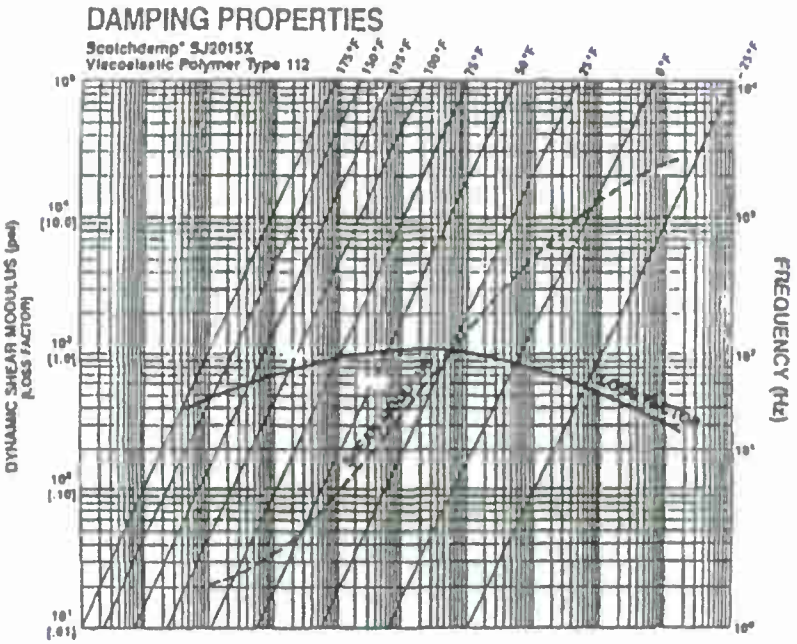


Figure 4.2: ISD-112 reduced frequency nomogram developed by 3M corporation[1].

## 4.5 Results

In order to begin to understand the power dissipation characteristics of different materials, a number of results were gathered using the analysis from section 4.4. The results to follow represent the response and power dissipation data pertinent to this work.

The materials chosen fall into two basic categories: (1) structural base materials and (2) damping material. For the structural base materials, research was conducted into materials commonly used for major structural applications. This includes: two grades of aluminum commonly found in aircraft structures, one alloy of structural grade titanium, one alloy of steel commonly found in maritime and assorted structural applications and two examples of fiberglass commonly found in watercraft and maritime structures. While fiberglass is technically a composite material, its properties were approximated to be isotropic (namely Poisson's ratio, elastic modulus, specific heat and coefficient of thermal conduction) as would approximately be the case for a chopped fiber configuration. The pertinent properties for all structural materials can be found in Table 4.1 courtesy of the MATWEB materials database[44].

For the damping material, 3M's ISD-112 polymer damping material was chosen. The reason for using this specific damping material was because of the extensive research performed on its properties over the past 40 years. ISD-112 has been used in many structural damping applications and as such, its loss factor and shear modulus as a function of frequency and temperature are very well understood. Figure 4.2 is the nomogram of ISD-112 as provided by 3M corporation.

This yields six combinations of base and damping material to be analyzed. What follows are the results of the CLD analysis utilizing these materials and the theory from section 4.4 as applied to these six systems. In each case the base plate is assumed to be 0.5 cm thick, 1 m long on

Table 4.1: The physical and thermal properties of the structural base materials used in comparing temperature rise information. All data gathered from[44]

| | Al 2024-T6 | Al 7075-T6 | AISI 1050 Steel | Ti Grade 23 | Premix 7203 | Premix 1203 |
|---|---|---|---|---|---|---|
| Poisson's Ratio | .33 | .33 | .29 | .342 | .3 | .3 |
| Bulk Density $\left[\frac{kg}{m^3}\right]$ | 2780 | 2810 | 7850 | 4430 | 1800 | 1950 |
| Elastic Modulus [GPa] | 72.4 | 71.7 | 205 | 113.8 | 15.2 | 15.2 |
| Thermal Conduction $\left[\frac{W}{m \cdot ^\circ C}\right]$ | 151 | 130 | 49.8 | 6.7 | .3 | .3 |
| Specific Heat $\left[\frac{J}{kg \cdot ^\circ C}\right]$ | 875 | 960 | 486 | 526 | 335 | 1510 |

each side and uniformly damped across its entire face. The constrained layer is assumed to be 1.5 mm thick 3M ISD-112 with a constraining layer of 1.5 mm thick AISI 1050 steel. The ISD-112 material is also assumed to be at 75 °F in evaluating material properties. Each combination has one figure displaying the driving point mobility transfer function and the driving point compliance transfer function as well as one table compiling pertinent results. These tables focus only on the power dissipation characteristics of the system while it is being excited at a modal frequency for the following reason. At a modal frequency, for a specified harmonic force, the response magnitude is always a local maximum. As the applied force magnitude is assumed to be constant for each case, only the velocity varies as a function of frequency. As the response is greatest at a modal frequency, so is the velocity and thus the power dissipation. For each base material/damping material combination and each of its first six modes, the plate is excited with the force that produces the maximum linear elastic response at the respective modal frequency.

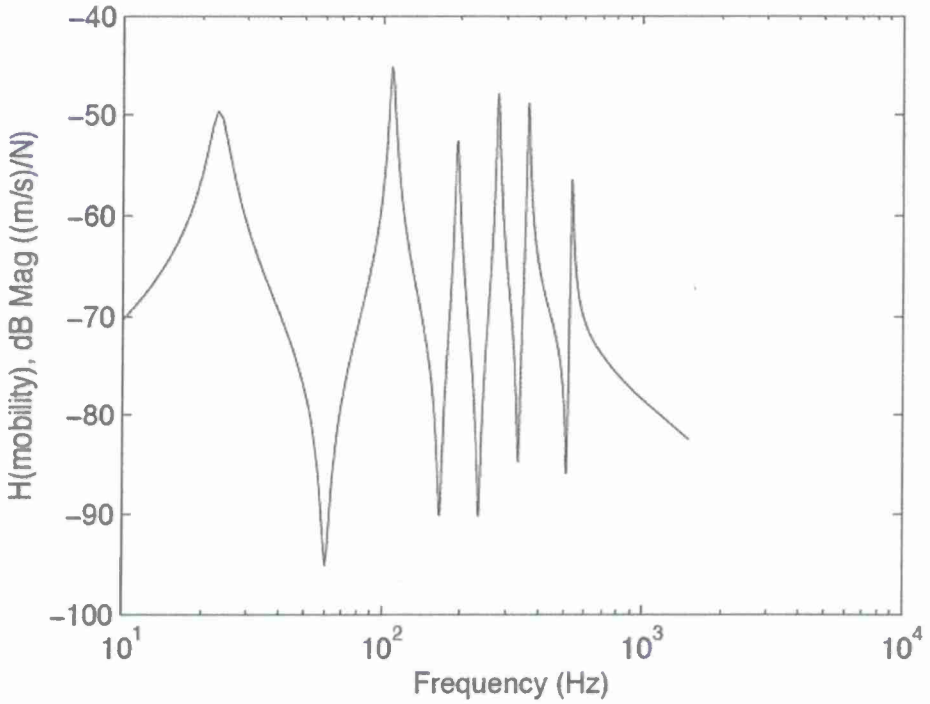


Figure 4.3: Mobility transfer function for first 6 modes of AISI 1050 steel base plate (0.5 cm thick) with AISI 1050 steel constraining layer (1.5 mm thick) and ISD-112 constrained layer (1.5 mm thick). Plate was forced harmonically at center with response measurement taken at forcing location. Plate dimensions: 1 m x 1 m.

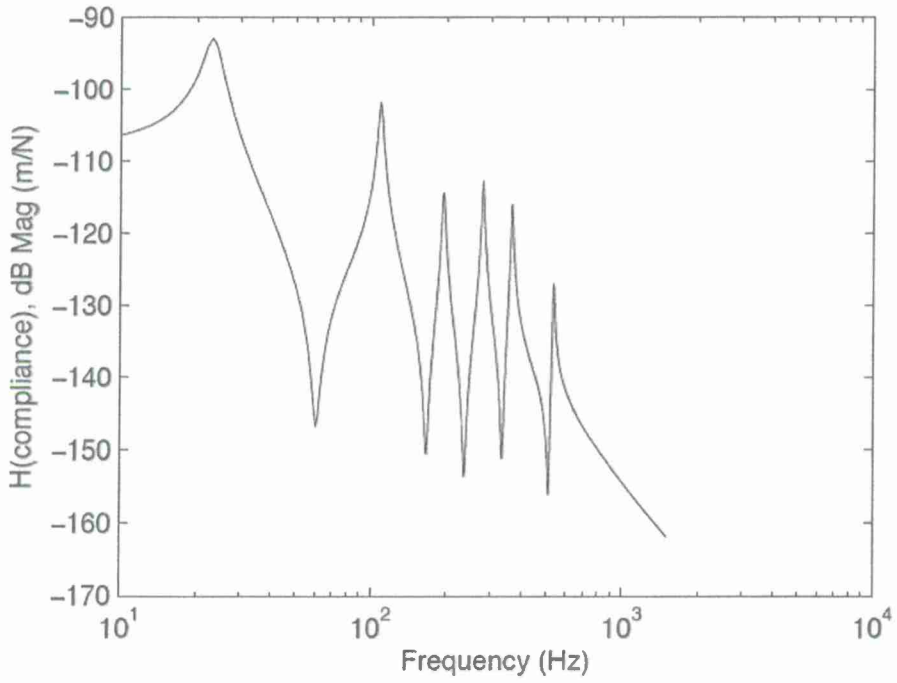


Figure 4.4: Compliance transfer function for first 6 modes of AISI 1050 steel base plate (0.5 cm thick) with AISI 1050 steel constraining layer (1.5 mm thick) and ISD-112 constrained layer (1.5 mm thick). Plate was forced harmonically at center with response measurement taken at forcing location. Plate dimensions: 1 m x 1 m.

| Mode | Freq [Hz] | Modal Loss Factor | $H_{comp,MAX}\left[\frac{\text{m}}{\text{N}}\right]$ | $F_{0,MAX}$ [N] | $P_{DIS}$ [W] |
|---|---|---|---|---|---|
| 1 | 23 | 0.1521 | $2.293 \times 10^{-5}$ | 3.49 | 0.0201 |
| 2 | 108 | 0.0417 | $8.193 \times 10^{-6}$ | 9.76 | 0.2631 |
| 3 | 193 | 0.0259 | $1.937 \times 10^{-6}$ | 41.30 | 1.9897 |
| 4 | 279 | 0.0197 | $2.334 \times 10^{-6}$ | 34.28 | 2.3594 |
| 5 | 364 | 0.0165 | $1.603 \times 10^{-6}$ | 49.91 | 4.4757 |
| 6 | 534 | 0.0169 | $4.489 \times 10^{-7}$ | 178.21 | 23.334 |

Table 4.2: Compiled results from Figures 4.3 and 4.4. The following is included for the first six modes: modal frequency, modal loss factor, maximum compliance transfer function value, excitation force required to bring plate to linear elastic limit and the power dissipation associated with linear elastic limit force.

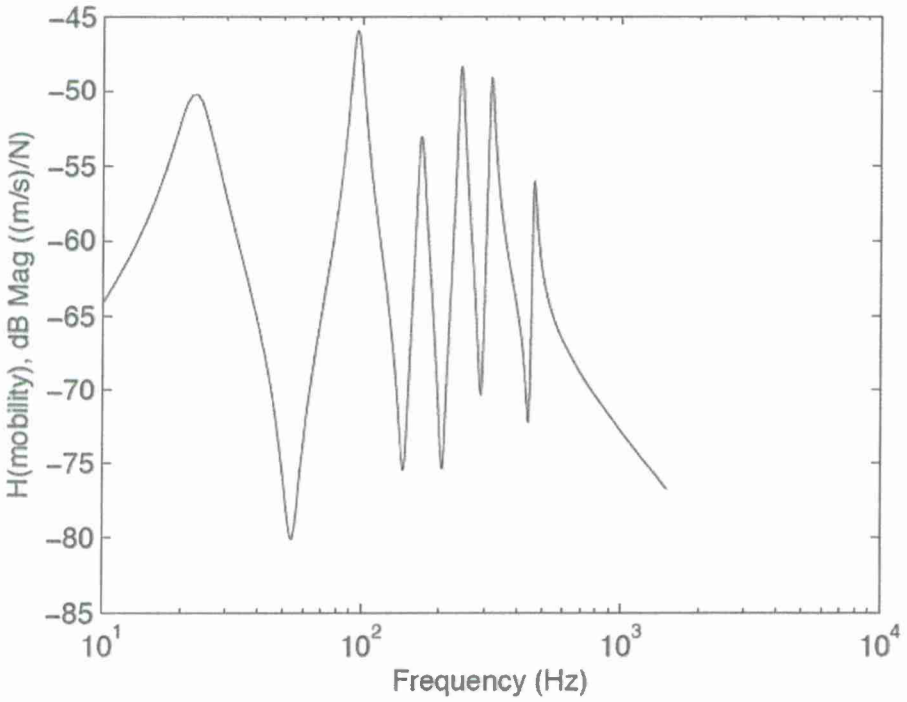


Figure 4.5: Mobility transfer function for first 6 modes of aluminum 2024-T6 base plate (0.5 cm thick) with AISI 1050 steel constraining layer (1.5 mm thick) and ISD-112 constrained layer (1.5 mm thick). Plate was forced harmonically at center with response measurement taken at forcing location. Plate dimensions: 1 m x 1 m.

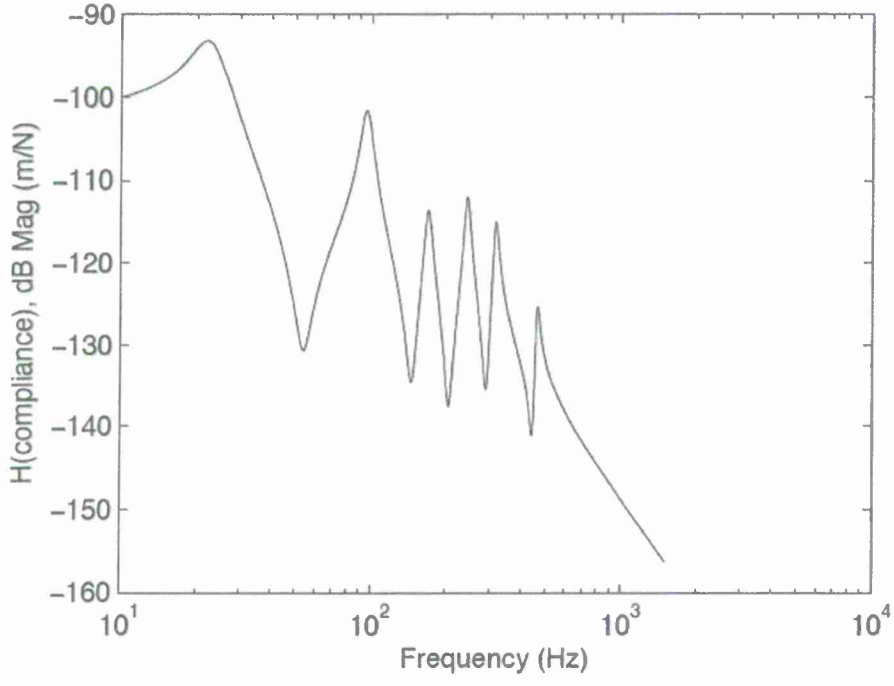


Figure 4.6: Compliance transfer function for first 6 modes of aluminum 2024-T6 base plate (0.5 cm thick) with AISI 1050 steel constraining layer (1.5 mm thick) and ISD-112 constrained layer (1.5 mm thick). Plate was forced harmonically at center with response measurement taken at forcing location. Plate dimensions: 1 m x 1 m.

| Mode | Freq [Hz] | Modal Loss Factor | $H_{comp,MAX}\ \left[\frac{\text{m}}{\text{N}}\right]$ | $F_{0,MAX}$ [N] | $P_{DIS}$ [W] |
|---|---|---|---|---|---|
| 1 | 22 | 0.3864 | $2.213 \times 10^{-5}$ | 3.62 | 0.0199 |
| 2 | 96 | 0.0938 | $8.366 \times 10^{-6}$ | 9.56 | 0.2301 |
| 3 | 169 | 0.0651 | $2.085 \times 10^{-6}$ | 38.37 | 1.6260 |
| 4 | 243 | 0.0576 | $2.513 \times 10^{-6}$ | 31.83 | 1.9187 |
| 5 | 317 | 0.0442 | $1.769 \times 10^{-6}$ | 45.22 | 3.3529 |
| 6 | 465 | 0.0430 | $5.409 \times 10^{-7}$ | 147.90 | 13.727 |

Table 4.3: Compiled results from Figures 4.5 and 4.6. The following is included for the first six modes: modal frequency, modal loss factor, maximum compliance transfer function value, excitation force required to bring plate to linear elastic limit and the power dissipation associated with linear elastic limit force.

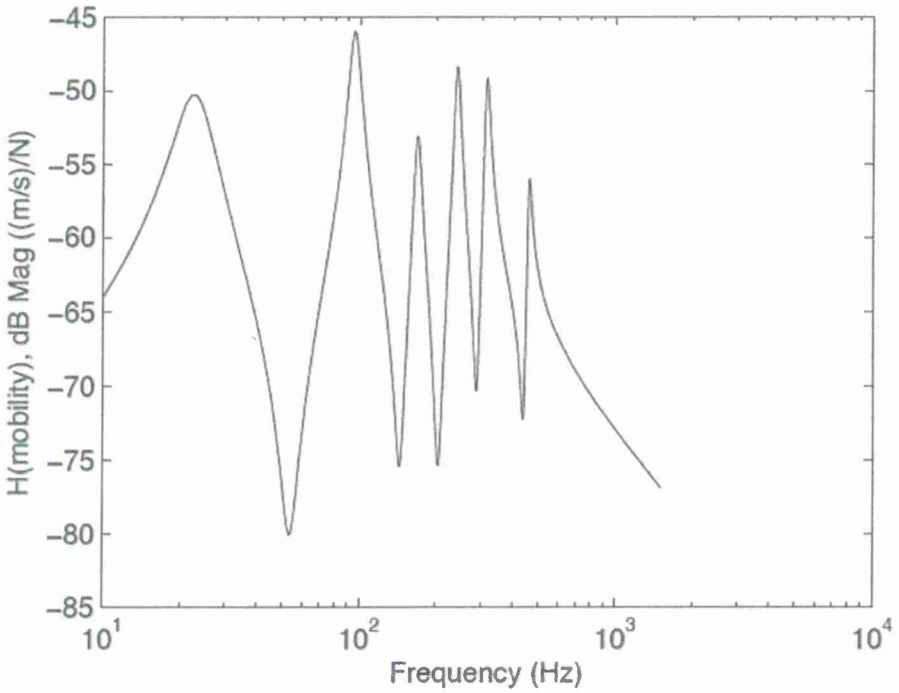


Figure 4.7: Mobility transfer function for first 6 modes of aluminum 7075-T6 base plate (0.5 cm thick) with AISI 1050 steel constraining layer (1.5 mm thick) and ISD-112 constrained layer (1.5 mm thick). Plate was forced harmonically at center with response measurement taken at forcing location. Plate dimensions: 1 m x 1 m.

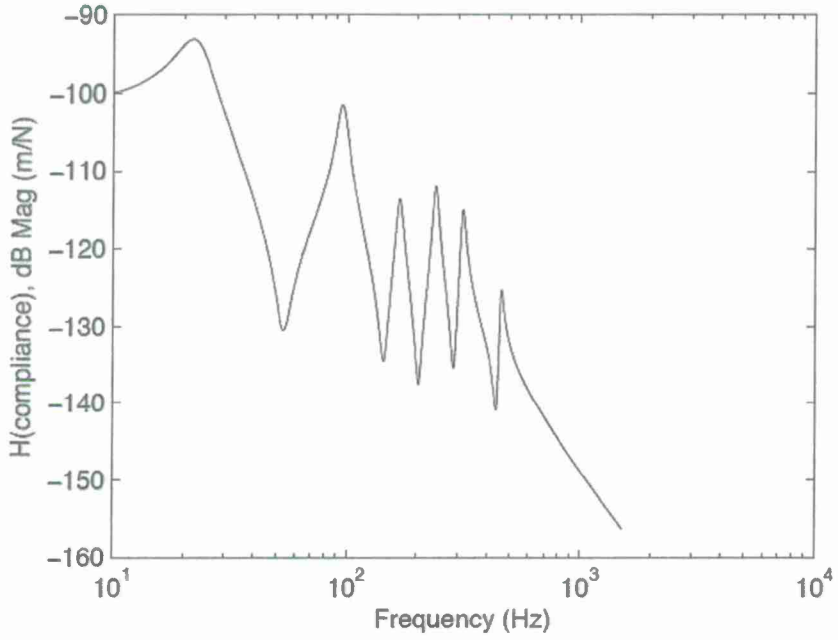


Figure 4.8: Compliance transfer function for first 6 modes of aluminum 7075-T6 base plate (0.5 cm thick) with AISI 1050 steel constraining layer (1.5 mm thick) and ISD-112 constrained layer (1.5 mm thick). Plate was forced harmonically at center with response measurement taken at forcing location. Plate dimensions: 1 m x 1 m.

| Mode | Freq [Hz] | Modal Loss Factor | $H_{comp,MAX}\left[\frac{\text{m}}{\text{N}}\right]$ | $F_{0,MAX}$ [N] | $P_{DIS}$ [W] |
|---|---|---|---|---|---|
| 1 | 22 | 0.3864 | $2.209 \times 10^{-5}$ | 3.62 | 0.0200 |
| 2 | 95 | 0.1000 | $8.406 \times 10^{-6}$ | 9.52 | 0.2274 |
| 3 | 168 | 0.0625 | $2.093 \times 10^{-6}$ | 38.22 | 1.6055 |
| 4 | 241 | 0.0498 | $2.527 \times 10^{-6}$ | 31.66 | 1.9045 |
| 5 | 315 | 0.0492 | $1.772 \times 10^{-6}$ | 45.15 | 3.2840 |
| 6 | 462 | 0.0433 | $5.430 \times 10^{-7}$ | 147.33 | 13.285 |

Table 4.4: Compiled results from Figures 4.7 and 4.8. The following is included for the first six modes: modal frequency, modal loss factor, maximum compliance transfer function value, excitation force required to bring plate to linear elastic limit and the power dissipation associated with linear elastic limit force.

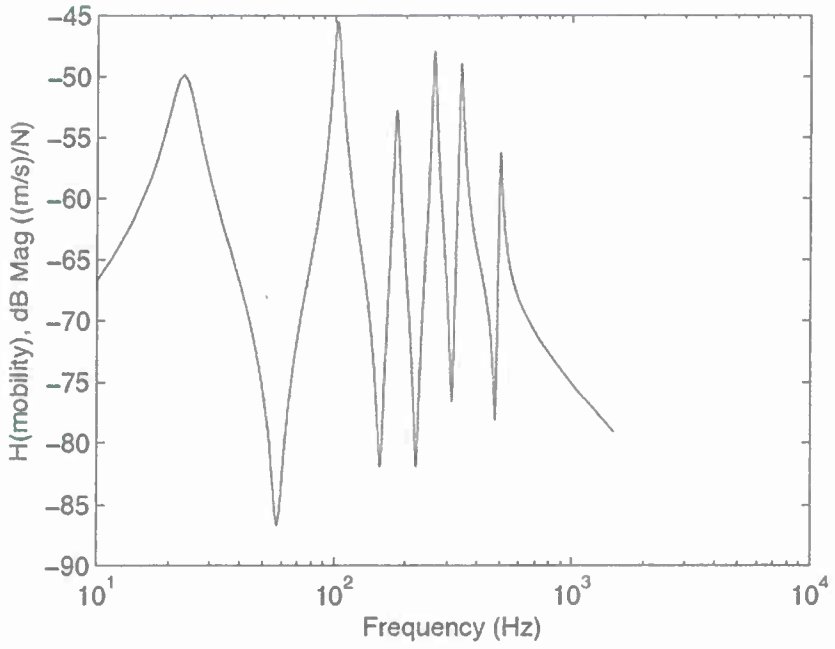


Figure 4.9: Mobility transfer function for first 6 modes of grade 23 titanium base plate (0.5 cm thick) with AISI 1050 steel constraining layer (1.5 mm thick) and ISD-112 constrained layer (1.5 mm thick). Plate was forced harmonically at center with response measurement taken at forcing location. Plate dimensions: 1 m x 1 m.

| Mode | Freq [Hz] | Modal Loss Factor | $H_{comp,MAX}\left[\frac{\text{m}}{\text{N}}\right]$ | $F_{0,MAX}$ [N] | $P_{DIS}$ [W] |
|---|---|---|---|---|---|
| 1 | 19 | 0.2826 | $2.229 \times 10^{-5}$ | 3.59 | 0.0071 |
| 2 | 99 | 0.0686 | $8.266 \times 10^{-6}$ | 9.68 | 0.1234 |
| 3 | 179 | 0.0412 | $2.015 \times 10^{-6}$ | 39.70 | 1.1529 |
| 4 | 257 | 0.0344 | $2.425 \times 10^{-6}$ | 32.99 | 1.0752 |
| 5 | 337 | 0.0292 | $1.671 \times 10^{-6}$ | 47.88 | 2.4456 |
| 6 | 496 | 0.0279 | $4.864 \times 10^{-7}$ | 164.47 | 13.339 |

Table 4.5: Compiled results from Figures 4.9 and 4.10. The following is included for the first six modes: modal frequency, modal loss factor, maximum compliance transfer function value, excitation force required to bring plate to linear elastic limit and the power dissipation associated with linear elastic limit force.

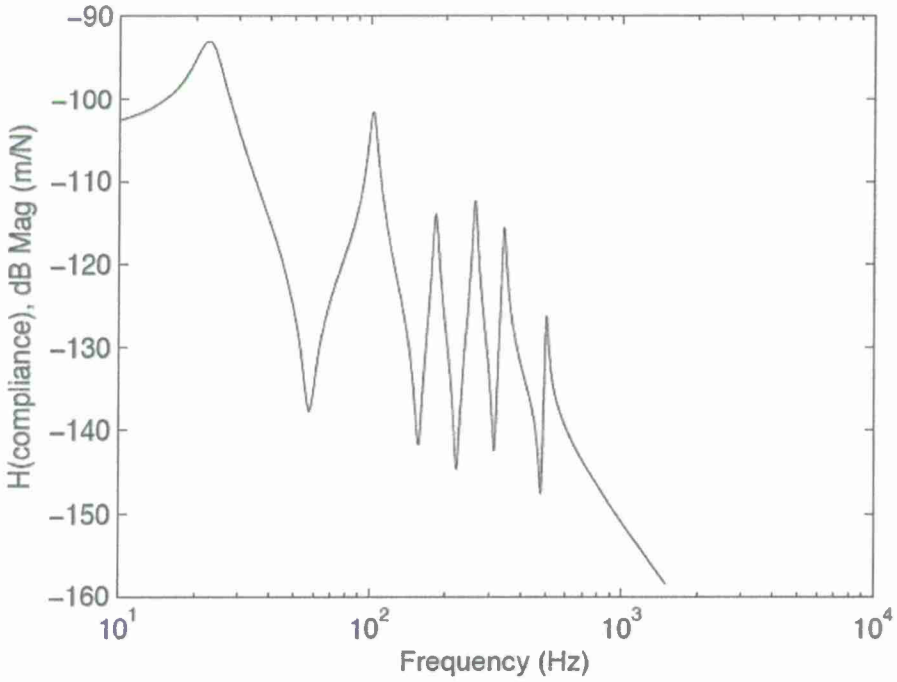


Figure 4.10: Compliance transfer function for first 6 modes of grade 23 titanium base plate (0.5 cm thick) with AISI 1050 steel constraining layer (1.5 mm thick) and ISD-112 constrained layer (1.5 mm thick). Plate was forced harmonically at center with response measurement taken at forcing location. Plate dimensions: 1 m x 1 m.

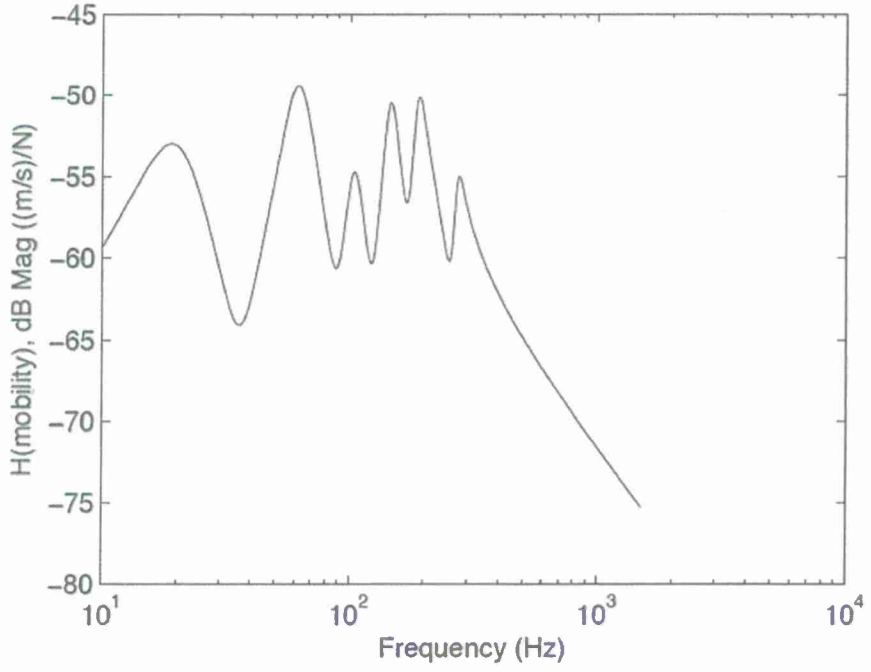


Figure 4.11: Mobility transfer function for first 6 modes of Premix 1203 base plate (0.5 cm thick) with AISI 1050 steel constraining layer (1.5 mm thick) and ISD-112 constrained layer (1.5 mm thick). Plate was forced harmonically at center with response measurement taken at forcing location. Plate dimensions: 1 m x 1 m.

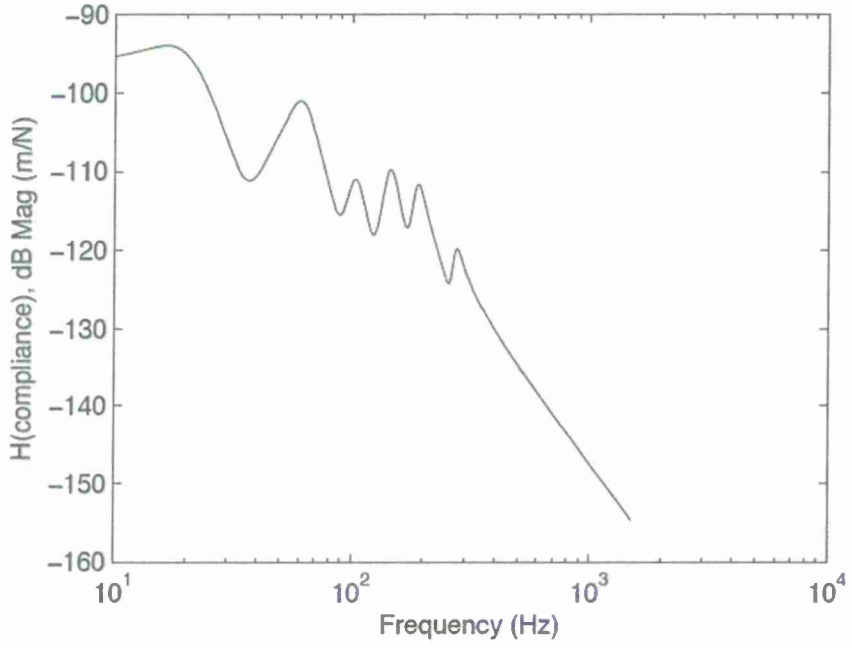


Figure 4.12: Compliance transfer function for first 6 modes of Premix 1203 base plate (0.5 cm thick) with AISI 1050 steel constraining layer (1.5 mm thick) and ISD-112 constrained layer (1.5 mm thick). Plate was forced harmonically at center with response measurement taken at forcing location. Plate dimensions: 1 m x 1 m.

| Mode | Freq [Hz] | Modal Loss Factor | $H_{comp,MAX}\left[\frac{\mathrm{m}}{\mathrm{N}}\right]$ | $F_{0,MAX}$ [N] | $P_{DIS}$ [W] |
|---|---|---|---|---|---|
| 1 | 16 | Undef | $2.140 \times 10^{-5}$ | 3.74 | 0.0131 |
| 2 | 60 | 0.2667 | $8.894 \times 10^{-6}$ | 8.99 | 0.1355 |
| 3 | 102 | 0.1667 | $2.819 \times 10^{-6}$ | 28.38 | 0.7098 |
| 4 | 143 | 0.1399 | $3.269 \times 10^{-6}$ | 24.47 | 0.8624 |
| 5 | 187 | 0.1337 | $2.612 \times 10^{-6}$ | 30.63 | 1.1368 |
| 6 | 272 | 0.1434 | $1.024 \times 10^{-6}$ | 78.13 | 2.8629 |

Table 4.6: Compiled results from Figures 4.11 and 4.12. The following is included for the first six modes: modal frequency, modal loss factor, maximum compliance transfer function value, excitation force required to bring plate to linear elastic limit and the power dissipation associated with linear elastic limit force.

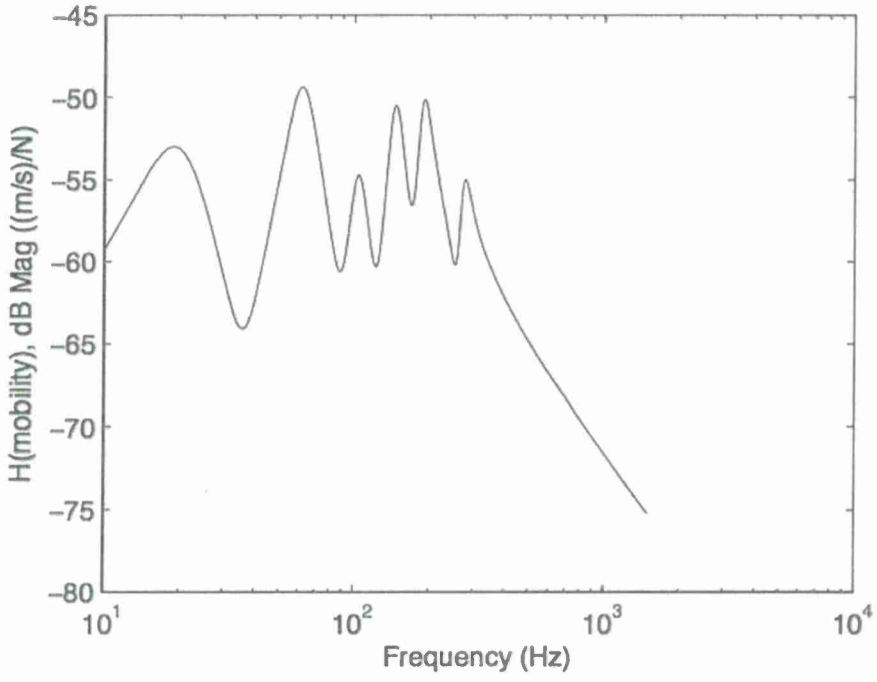


Figure 4.13: Mobility transfer function for first 6 modes of Premix 7203 base plate (0.5 cm thick) with AISI 1050 steel constraining layer (1.5 mm thick) and ISD-112 constrained layer (1.5 mm thick). Plate was forced harmonically at center with response measurement taken at forcing location. Plate dimensions: 1 m x 1 m.

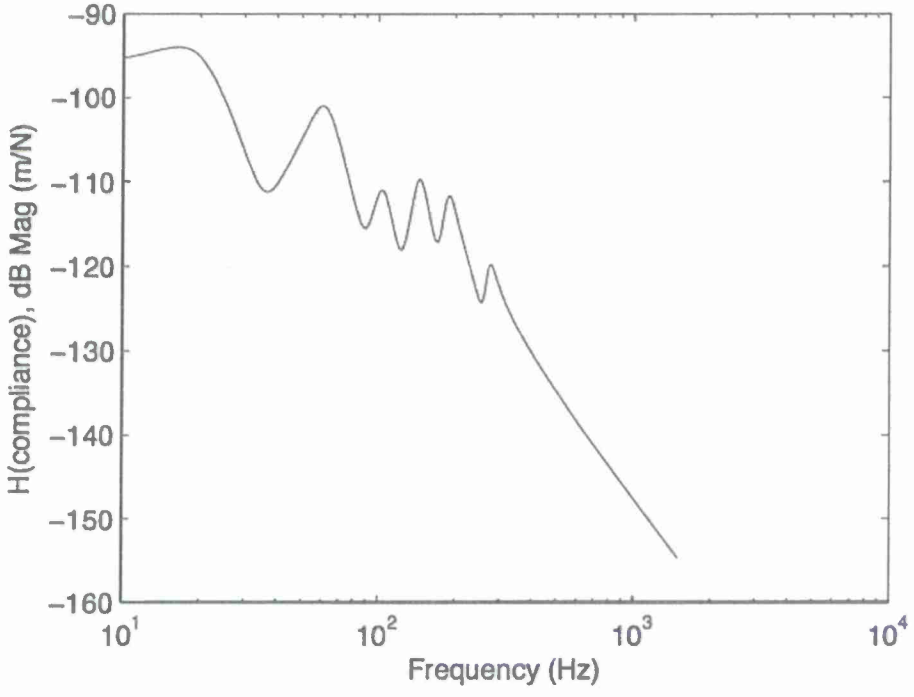


Figure 4.14: Compliance transfer function for first 6 modes of Premix 7203 base plate (0.5 cm thick) with AISI 1050 steel constraining layer (1.5 mm thick) and ISD-112 constrained layer (1.5 mm thick). Plate was forced harmonically at center with response measurement taken at forcing location. Plate dimensions: 1 m x 1 m.

| Mode | Freq [Hz] | Modal Loss Factor | $H_{comp,MAX}\ \left[\frac{\mathrm{m}}{\mathrm{N}}\right]$ | $F_{0,MAX}$ [N] | $P_{DIS}$ [W] |
|---|---|---|---|---|---|
| 1 | 16 | Undef | $2.010 \times 10^{-5}$ | 3.98 | 0.0149 |
| 2 | 60 | 0.2833 | $8.891 \times 10^{-6}$ | 9.00 | 0.1358 |
| 3 | 103 | 0.1748 | $2.813 \times 10^{-6}$ | 28.44 | 0.7013 |
| 4 | 146 | 0.1370 | $3.254 \times 10^{-6}$ | 24.59 | 0.8056 |
| 5 | 190 | 0.1368 | $2.602 \times 10^{-6}$ | 30.75 | 0.9715 |
| 6 | 276 | 0.1413 | $1.020 \times 10^{-6}$ | 78.43 | 2.2860 |

Table 4.7: Compiled results from Figures 4.13 and 4.14. The following is included for the first six modes: modal frequency, modal loss factor, maximum compliance transfer function value, excitation force required to bring plate to linear elastic limit and the power dissipation associated with linear elastic limit force.

## 4.6 Discussion of Results

The results acquired in this analysis provide some interesting insight into the response of CLD treatment systems. One of the most noticeable results in this analysis is how power dissipation rises with the mode number in almost every case. The reason for this can be intuitively determined. As mode number increases, it can be seen that, generally, the force required to push the plate to its linear elastic limit at a modal frequency also increases. Studying the compliance transfer function leads to the conclusion that if force magnitude is held constant while the modal excitation frequency is increased, the maximum dispacement follows a decreasing trend. In order to maintain the displacement at the plate's linear elastic limit - 1% of the plate's thickness - then force magnitude must instead increase with modal frequency. Studying the mobility transfer function we can similarly assume that, as this excitation force increases so does velocity. As expected the power is known to vary directly with the product of forcing magnitude and velocity. If the forcing magnitude and velocity have increasing trends, then so must the power dissipation. Both the mobility and transfer function must be studied in order to observe this relationship. Characterizing the trend in power dissipation based only on the mobility or compliance transfer function leads to incorrect trends in power dissipation. This increase in power dissipated on a per unit volume basis can be seen in Table 4.8.

Figure 4.8 also allows the comparison of power dissipated per unit volume to be compared across the six different systems. The power dissipation terms in individual modes tend to stay on the same order of magnitude regardless of base material chosen in the first few modes. As mode numbers rise, power dissipation tends to increase with density and elastic modulus of the material. This can be seen to be the case with all materials, especially in mode six. Here power dissipation is highest in steel (highest density and elastic modulus) and lowest in the fiberglass composites (lowest density and elastic modulus) with titanium and the aluminum alloys falling somewhere between these other materials, both in material properties and power dissipation terms. Section ?? of this work presents a unified analysis using these power dissipation terms and a temperature profiling analysis to be conducted in section ??.

Table 4.8: Power dissipated per unit volume of damping material for all base materials with ISD-112 viscoelastic CLD material for first six modes of vibration. Material and geometric conditions detailed in section 4.5. Power dissipation corresponds to excitation at modal frequencies at vibration linear elastic limit.

| Mode | Al 2024-T6 | Al 7075-T6 | AISI 1050 Steel | Ti Grade 23 | Premix 7203 | Premix 1203 |
|---|---|---|---|---|---|---|
| 1 | 13 | 13 | 13 | 5 | 10 | 9 |
| 2 | 153 | 152 | 175 | 82 | 91 | 90 |
| 3 | 1084 | 1070 | 1326 | 769 | 468 | 473 |
| 4 | 1279 | 1270 | 1573 | 717 | 537 | 575 |
| 5 | 2235 | 2189 | 2984 | 1630 | 648 | 758 |
| 6 | 9151 | 8857 | 15556 | 8893 | 1524 | 1909 |

# Bibliography


[1] Ping Hsin-Chih. *Passive vibration control of thick aluminum plates using viscoelastic layered damping.* PhD thesis, Naval Post-Graduate School, 1990.

[2] Y. Maeda, S. Nishiwaki, K. Izui, M. Yoshimura, K. Matsui, and K. Terada. Structural topology optimization of vibrating structures with specified eigenfrequencies and eigenmode shapes. *International Journal for Numerical Methods in Engineering*, 67:597–628, 2006.

[3] Lei Shu, Michael Yu Wang, Zongde Fang, Zhengdong Ma, and Peng Wei. Level set based structural topology optimization for minimizing frequency response. *Journal of Sound and Vibration*, 330:5820–5834, 2011.

[4] Mohammad A. Heidari. Optimization of peak power in vibrating structures via semidefinite programming. In *Proceedings of the 2009 AIAA/ASME/ASCE/AHS/ASC Structures, Structural Dynamics, and Materials Conference.*, 2009.

[5] Magnus Alvelid. Optimal position and shape of applied damping material. *Journal of Sound and Vibration*, 310:947–965, 2008.

[6] H. Zheng, G.S.H. Pau, and Y.Y. Wang. A comparative study on optimization of constrained layer damping a comparative study on optimization of constrained layer damping treatment for structural vibration control. *Thin-Walled Structures*, 44:886–896, 2006.

[7] Walter Ritz. Theorie der Transversalschwingungen einer quadratischen Platte mit freien Rändern. *Annalen der Physik*, 228:737–786, 1909.

[8] William Rowan Hamilton. On a General Method in Dynamics. *Philosophical Transactions of the Royal Society, Part II*, pages 247–308, 1834.

[9] William Rowan Hamilton. Second Essay on a General Method in Dynamics. *Philosophical Transactions of the Royal Society of London, Part I*, 125:95–144, January 1835.

[10] Jerry H. Ginsberg. *Mechanical and Structural Vibrations.* John Wiley & Sons, Inc., New York, New York, 2001.

[11] Singiresu Rao. *Vibration of Continuous Systems.* John Wiley & Sons, Inc., Hoboken New Jersey, 2007.

[12] G.M. Oosterhout, P.J.M van Der Hoogt, and R.M.E.J. Spiering. Accurate calculation methods for natural frequencies of plates with special attention to the higher modes. *Journal of Sound and Vibration*, 183(1):33–47, May 1995.

[13] R.J. McQuillin and E.M. Kerwin Jr. Effectiveness of 'patches' of treatment in the damping of flexural waves in systems. In *Sixty-Fourth Meeting of the Acoustical Society of America*, volume 34, page 1977. Acoustical Society of America, 1962.

[14] R.J. McQuillin and E.M. Kerwin Jr. Damping of flexural waves by 'patches' of treatment. In *Sixty-First Meeting of the Acoustical Society of America*, volume 33, page 861, 1961.

[15] I. Takewaki. Optimal damper placement for minimum transfer function. *Earthquake Engineering & Structural Dynamics*, 26(11):1113–1124, 1997.

[16] Tudor Sireteanu and Nicolae Stoia. Damping optimization of passive and semi-active vehicle suspension by numerical simulation. volume 4, pages 1–7. The Publishing House of the Romainian Academy, 2003.

[17] H. Zheng, C. Cai, G.S.H. Pau, and G.R. Liu. Minimizing vibration response of cylindrical shells through layout optimization of passive constrained layer damping treatments. *Journal of Sound and Vibration*, 279:739–756, 2005.

[18] Gian Paolo Cimellaro. Simultaneous stiffness–damping optimization of structures with respect to simultaneous stiffness–damping optimization of structures with respect to acceleration, displacement and base shear. *Engineering Structures*, 29:2853–2870, 2007.

[19] A.L. Araújo, C.M. Mota Soares, C.A. Mota Soares, and J. Herskovits. Damping optimization of viscoelastic laminated sandwich composite structures. In *EngOpt 2008 - International Conference on Engineering Optimization*, Rio de Janeiro, Brazil, June 2008.

[20] D.R. Morgenthaler. The absolute modal strain energy method. In *Proceedings of Damping '91*, volume 2, pages FDB 1–16. Wright Laboratory Flight Dynamics Directorate, 1991.

[21] C.D. Johnson, D.A. Kleinholz, and L.C. Rogers. Finite element prediction of damping in beams with constrained viscoelastic layers. *Shock and Vibration Bulletin*, 51(1):71–81, 1981.

[22] J. Gregory McDaniel and Jerry H. Ginsberg. Fundamental tests of two modal strain energy methods. *Journal of Vibration and Acoustics*, 118(2):272–275, 1996.

[23] James R. Lhota Steven M. Shepard, Tasdiq Ahmed. Experimental considerations in vibrothermography. *Proceedings of SPIE, Thermosense*, 5405:332–335, 2004.

[24] E.M. Zanetti A.L. Audenino, V. Crupi. Correlation between thermography and internal damping in metals. *International Journal of Fatigue*, 25:343–351, 2002.

[25] D.A. Lunsford K. Kasai K.C. Chung M.L. Lai, P. Lu. Viscoelastic damper: A damper with linear or non-linear material. In *Eleventh World Conference of Earthquake Engineering*, 1996.

[26] Edward M. Kerwin. Damping of flexural waves by a constrained viscoelastic layer. *Journal of the Acoustical Society of America*, 31:952–962, 1959.

[27] R.A. DiTaranto. Theory of vibratory bending for elastic and viscoelastic layered finite-length beams. *Journal of Applied Mechanics*, 32:881–886, 1965.

[28] Eric E. Ungar Donald Ross and E.M. Kerwin. Damping of plate flexural vibrations by means of viscoelastic laminae. *ASME, Structural Damping*, pages 49–88, 1959.

[29] Y.V.K. Rao and B.C. Nakra. Vibrations of unsymmetrical sandwich beams and plates with viscoelastic cores. *Journal of Sound and Vibration*, 34:309–326, 1974.

[30] R.A. DiTaranto and J.R. McGraw. Vibratory bending of viscoelastically damped laminated structures. *Journal of Engineering for Industry, Transactions of ASME*, 91:1081–1090, 1969.

[31] Y. Y. Yu. Damping of flexural vibrations of sandwich plates. *Journal of Aerospace Sciences*, 29:790–803, 1962.

[32] Y.P. Lu C.T. Sun. *Vibration and Damping of Structural Elements.* Prentice Hall, 1995.

[33] Y.V.K. Rao and B.C. Nakra. Theory of vibratory bending of unsymmetrical sandwich plates. *Archives of Mechanics*, 25:213–225, 1973.

[34] G.C. Everstine Y.P. Lu, J.W. Killian. Vibrations of three layered damped sandwich plate composites. *Jounral of Sound and Vibration*, 64:63–71, 1979.

[35] J.W. Killian and Y.P. Lu. A finite element modeling approximation for damping material used in constrined damped structures. *Journal of Sounds and Vibration*, 97:352–354, 1984.

[36] R.F. Gibson and R. Plunkett. Dynamic mechanical behavior of fiber reinforced composites; measurements and analysis. *Journal of Composite Materials*, 10:325–341, 1976.

[37] J.K. Wu C.T. Sun and R.F. Gibson. Prediction of material damping in randomly oriented short-fiber polymer matrix composites. *Jounral of Reinforced Plastics and Composites*, 4:262–272, 1985.

[38] J.C. Jaegar H.S. Carslaw. *Conduction of Heat in Solids.* Oxford University Press, 1959.

[39] S.S. Russell and E.G. Henneke. Dynamic effects during vibrothermographic non-destructive evaluation of composites. *NDT International*, 17:19–25, 1984.

[40] Stephen D. Holland Jeremy Renshaw and R. Bruce Thompson. Measurement of crack opening stresses and crack closure stress profiles from heat generation in vibrating cracks. *Applied Physics Letters*, 93:081914, 2008.

[41] Daniel J. Barnard Jeremy Renshaw, Stephen D. Holland. Viscous material filled synthetic defects for vibrothermography. *NDT&E International*, 42:753–756, 2009.

[42] E.M. Zanetti A.L. Audenino, V. Crupi. Thermoelastic and elastoplastic effects measured by means of a standard thermocamera. *Experimental Techniques*, 28:23–28, 2004.

[43] M.L. Lai H.S. Gopalakrishna. Finite element heat transfer analysis of viscoelastic damper for wind applications. *Jounral of Wind Engineering and Industrial Aerodynamics*, 77:283–295, 1998.

[44] MatWeb. Materials property database.

[45] Jerry H. Ginsberg. *Mechanical and Structural Vibrations: Theory and Applications.* Wiley Publications, 2001.

[46] D.J. Mead and S. Markus. Loss factors and resonant frequencies of encastre damped sandwich beams. *Journal of Sound and Vibration*, 12:99–112, 1970.

[47] D.J. Mead and S. Markus. The forced vibration of a three-layer, damped sandwich beam with arbitrary boundary conditions. *Journal of Sound and Vibration*, 10:163–175, 1969.

[48] Y.V.K. Rao. *Vibrations of unsymmetrical sandwich structures.* PhD thesis, Indian Institute of Technology, Delhi, 1972.

[49] Werner Soedel. *Vibrations of Plates and Shells.* Marcel Dekker Inc., 2004.

[50] M.J. Yan and E.H. Dowell. Governing equations for vibrating constrained-layer damping sandwich plates and beams. *Jounrnal of Applied Mechanics*, pages 1041–1046, 1972.

[51] Joel Garrelick. Boundary damping of flexural vibrations in beams and plates. In *145th Meeting of the Acoustical Society of America*, volume 113, April 2003.

[52] N.F.J. van Rensburg, A.J. van der Merwe, and A. Roux. Waves in a vibrating solid with boundary damping. *Wave Motion*, 47:663–675, 2010.